Single-Phase Inverter Virtual Oscillator-Based Grid-Forming Control for Distributed Energy Resources

Muhannad Mohammad Alluhaydan

Supervisor: Georgios Konstantinou

muhannad.alluhaydan@kaust.edu.sa g.konstantinou@unsw.edu.au

Abstract

The increasing penetration of inverter-based resources (IBRs) is reducing the rotational inertia traditionally provided by synchronous generators and making weak grids more sensitive to disturbances. Grid-forming (GFM) control addresses this challenge by allowing inverters to establish and regulate voltage and frequency as controlled voltage sources rather than relying on an existing grid waveform. This practicum compares two single-phase virtual oscillator control (VOC) methods: a Van der Pol oscillator-based VOC and the Integrated Andronov–Hopf Oscillator (IAHO). Both controllers were implemented in PLECS using the same 10 kVA, 230 V, 50 Hz inverter and tested under identical islanded and grid-connected conditions, including black start, load changes, grid synchronisation, active-power steps, grid-frequency disturbances and voltage sags. The Van der Pol controller maintains very small frequency deviations in islanded operation but shows larger voltage variations and more oscillatory grid-connected behaviour. In contrast, the IAHO synchronises faster, provides better damping, responds faster to active-power changes, gives stronger active-power support during grid-frequency disturbances and produces lower low-order voltage THD. During the voltage-sag test, the Van der Pol implementation provides stronger voltage support because of its additional volt-var control loop. Overall, the Van der Pol VOC is simpler and performs well in islanded operation, while the IAHO provides better dynamic and grid-support performance in the tested weak-grid system. The study is simulation-based and does not include experimental validation.

DATE	August 17, 2026
HOST INSTITUTION	UNSW Sydney, Australia
SIMULATION PLATFORM	PLECS

Contents

Nomenclature ... 3
1 Introduction ... 5
2 Related Work ... 5
2.1 Grid-following and grid-forming control ... 5
2.2 Droop and virtual synchronous machine control ... 5
2.3 Virtual oscillator control ... 5
2.4 Virtual inertia in Andronov–Hopf oscillators ... 6
2.5 Single-phase damping-enhanced AHO ... 6
2.6 Integrated Andronov–Hopf oscillator ... 6
2.7 Research gap addressed by this practicum ... 6
3 Methodology ... 6
3.1 Overall practicum workflow ... 6
3.2 Single-phase inverter model ... 7
3.3 Single-phase SOGI-based quadrature signal generation ... 9
3.4 Van der Pol VOC ... 10
3.5 Van der Pol parameter selection ... 11
3.6 Grid pre-synchronisation and static transfer switch logic ... 12
3.7 Andronov–Hopf oscillators and virtual inertia ... 13
3.8 IAHO controller ... 14
3.9 Feedforward damping controller synthesis ... 16
3.10 SOGI-FLL-based grid-frequency estimation ... 17
3.11 IAHO reactive-power–voltage droop and voltage support ... 17
3.12 Current limiting via virtual impedance ... 18
3.13 IAHO parameter design and scaling ... 18
3.14 Matched-plant comparison methodology ... 21
3.15 Disturbance scenarios ... 24
3.16 Performance metrics and post-processing ... 24
4 Results ... 25
4.1 Van der Pol baseline behaviour ... 25
4.2 Van der Pol design-relation study ... 25
4.3 IAHO design-relation study ... 26
4.4 Islanded black start ... 27
4.5 Islanded load step ... 29
4.6 Pre-synchronisation and STS closure ... 30
4.7 Grid-connected active-power step ... 31

4.8 Grid frequency disturbance 32
4.9 Grid voltage sag 33
4.10 Low-order steady-state voltage harmonic content 35
4.11 Current stress and modulation utilisation 36
4.12 Overall performance summary 37
5 Discussion 37
5.1 Island-mode interpretation 38
5.2 Grid-connected active-power interpretation 38
5.3 Frequency-support interpretation 38
5.4 Voltage-sag interpretation 38
5.5 Unexpected findings 38
5.6 Influence of SOGI dynamics and frequency estimation 39
5.7 Role of current protection 39
5.8 Grid-strength dependence and controller complexity 39
5.9 Controller selection and application suitability 39
6 Limitations and Future Work 40
7 Conclusion 41
References 41

Nomenclature

Symbol	Meaning
S_n, V_n, f_n	Rated apparent power, nominal RMS voltage, nominal frequency
V_{dc}, f_{sw}, f_{ctrl}	DC-link voltage, switching frequency, control frequency
L_1, C_f, R_d, L_2	LCL filter inductors, capacitor and damping resistor
R_T, X_T, K_s	Total path resistance, reactance, and small-signal synchronising power (power-angle) coefficient
v, i_{Lv}	Van der Pol oscillator voltage and internal tank current
κ_v, κ_i	Van der Pol voltage and current scaling factors
σ, α	Negative conductance and cubic coefficient
C, L, ε	Virtual capacitance, inductance and nonlinearity parameter
V_{oc}, V_{min}	Open-circuit and rated-load RMS voltage
m_P, m_Q	Van der Pol active and reactive droop slopes
λ_A, P_{crit}	Amplitude pole and stability limit
δ_{31}	Third-to-first harmonic ratio
v_α, v_β, V_p	AHO state components and amplitude
V_{p0}, μ, η	Nominal amplitude, AHO amplitude gain, and IAHO current-tracking / active-power droop gain
m_q, R_{droop}	Reactive droop slope, droop percentage
T_f, ω_f, H_{eq}	Inertial lag, its bandwidth, equivalent inertia constant
T_{so}, K_{so}	SOGI equivalent lag and gain
ξ_{FLL}, $\omega_{n\text{-}FLL}$	SOGI-FLL damping factor and natural frequency
$G_p(s)$, $G_\omega(s)$	Feedforward damping controllers
$G_R(s)$,$y'_{\alpha\beta}$	Resonant inertia controller and its output
ζ, ω_{n1}, ω_{n2}	Desired damping factor and natural frequencies
ω_0, ω_0', $\hat{\omega g}$	Nominal, corrected and estimated grid frequency
δ, θ	Power angle and oscillator phase
P, Q, P_{ref}, Q_{ref}	Active and reactive power and their references
i_L, i_g	Inverter-side and grid-side current
v_{pcc}, v_{inv}	PCC voltage and inverter bridge output voltage
I_{th}, R_v, X_v	Current threshold and virtual impedance components
φ, φ_Z, λ_{11}	Coupling rotation, tie angle, RGA diagonal
SCR	Short-circuit ratio
RoCoF	Rate of change of frequency
GFM, VOC, AHO	Grid-forming, virtual oscillator control, Andronov–Hopf oscillator

Symbol	Meaning
STS, SOGI, FLL	Static transfer switch, second-order generalised integrator, frequency-locked loop
IBR, GFL	Inverter-based resource, grid-following
PLL, PCC	Phase-locked loop, point of common coupling
QSG, PWM	Quadrature signal generator, pulse-width modulation
PI, VSM	Proportional–integral controller, virtual synchronous machine
THD, APL	Total harmonic distortion, active-power loop
VI-AHO, Da-AHO	Virtual-inertia AHO, damping-enhanced AHO
EAHO, uVOC	Enhanced AHO, unified virtual oscillator control

1 Introduction

PV, wind and battery storage are steadily displacing synchronous generation and, with it, the rotational inertia traditionally supplied by rotating machines. Grid-forming (GFM) inverters address this transition by establishing voltage and frequency rather than following an existing grid waveform, which is relevant to small single-phase distributed energy resources as well as utility-scale plants [1], [2].

A conventional grid-following inverter behaves mainly as a controlled current source and relies on a phase-locked loop (PLL) for synchronisation. It therefore cannot independently establish the voltage and frequency of an islanded network and can exhibit reduced robustness under weak-grid conditions. GFM control instead regulates the converter terminal voltage, enabling islanded operation, black start, synchronisation and direct voltage or frequency support.

Virtual oscillator control (VOC) builds the inverter voltage directly from nonlinear oscillator dynamics, and the primary oscillator synchronises through electrical feedback alone, with no PLL. Single phase makes this harder: orthogonal $\alpha\beta$ quantities have to be generated wherever they are needed, and the 100 Hz power ripple has to be filtered, both of which add measurement dynamics to the loop.

The comparison made here places a hierarchical Van der Pol controller and the Integrated Andronov-Hopf Oscillator (IAHO) on the same 10 kVA, 230 V, 50 Hz PLECS plant. Their channel pairings differ: Van der Pol pairs P→V and Q→ω, whereas the IAHO adopts the machine-like P→ω and Q→V pairing and adds virtual inertia, feedforward damping and voltage-independent active-power droop [1]. Six tests cover black start, islanded loading, synchronisation, active-power dispatch, a grid-frequency disturbance and a voltage sag. Scope is one simulated inverter with an ideal 500 V DC source; multi-inverter operation and hardware validation are outside the scope.

2 Related Work

2.1 Grid-following and grid-forming control

Grid-following control derives its current injection from a PLL angle and therefore requires an externally established voltage waveform. It cannot independently form an islanded network, does not inherently provide inertial response, and can lose robustness as grid strength decreases. Grid-forming control regulates its own terminal-voltage magnitude and angle, enabling black start, islanded operation and direct grid support.

2.2 Droop and virtual synchronous machine control

Droop control imposes P–f and Q–V characteristics around inner converter loops; virtual synchronous machine (VSM) control goes further and emulates the swing equation, providing inertia and damping. Both are well established, and both keep a layered control structure.

2.3 Virtual oscillator control

VOC takes a different route, generating the inverter voltage from nonlinear oscillator dynamics and synchronising without communication. Early work demonstrated rapid self-synchronisation and power sharing [3], [4]; later work extended the idea to dispatchable and grid-compatible oscillator families [5]–[7], [13].

Van der Pol is the usual choice of oscillator core, since its cubic nonlinearity settles onto a stable limit cycle. Hierarchical implementations add secondary voltage and frequency regulation, pre-synchronisation and tertiary P/Q tracking [4], [8].

The Andronov-Hopf oscillator (AHO) uses a norm-based isotropic nonlinearity instead. That avoids the Van der Pol cubic third-harmonic mechanism and gives a convenient $\alpha\beta$ structure for dispatchable grid-forming control [5], [7], [9].

2.4 Virtual inertia in Andronov–Hopf oscillators

Luo et al. [10] added virtual inertia to the AHO through a resonant current-feedback path whose averaged response behaves as a first-order lag. RoCoF falls as a result, but the system order rises and damping can suffer.

2.5 Single-phase damping-enhanced AHO

Rezazadeh et al. [11] addressed this damping loss for single-phase AHO control, using feedforward terms driven by the active-power reference and the estimated grid frequency. Their model also keeps the dynamic effect of the single-phase SOGI rather than assuming it is ideal.

2.6 Integrated Andronov–Hopf oscillator

EAHO [12] focused on removing the voltage dependence of the active-power droop coefficient so that droop stays consistent while voltage varies, but without virtual inertia or damping enhancement.

The IAHO [1] brings the three together: resonant virtual inertia, feedforward damping enhancement and voltage-independent active-power droop in one single-phase controller. Its published validation is on a 2.5 kVA converter and compares AHO variants, not a Van der Pol VOC.

2.7 Research gap addressed by this practicum

Van der Pol VOC and the AHO family have generally been benchmarked against different baselines [1], [4], [10], [11], so a direct comparison on one single-phase plant is useful, provided the shared electrical conditions and the remaining implementation asymmetries are stated explicitly.

This practicum implements, scales and tunes both families on a common 10 kVA platform. The tested network is also weaker and more resistive than the published IAHO case (R_T/X_T = 1.05, SCR ≈ 1.4), so network dependence is retained in the interpretation.

3 Methodology

3.1 Overall practicum workflow

Work proceeded in three phases (Figure 1): establish the Van der Pol baseline, implement the IAHO on the same plant, and then match the external conditions before comparison.

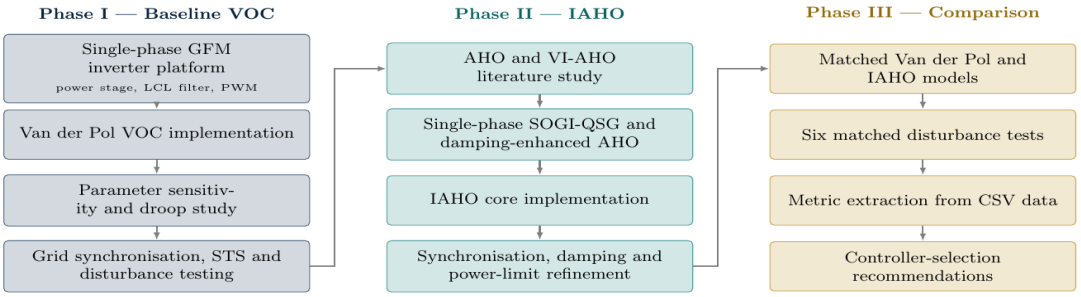


Figure 1 Development workflow. Phase I built a working Van der Pol baseline, Phase II added the IAHO on the same power stage, and Phase III matched the two models before identical disturbances were applied.

Phase I covered the single-phase plant, the Van der Pol VOC itself, its parameter design, synchronisation and STS logic. Phase II worked through the AHO literature (conventional AHO, then virtual inertia, then damping enhancement, then IAHO) while leaving the validated power stage untouched. Phase III aligned references and event timing, ran the six disturbance tests and extracted the common metrics.

Table 1 lists the development steps that survive in the final models.

Table 1 Development timeline, reconstructed from the design records kept in the final PLECS models.

Phase	Step	Outcome
I	Power stage	10 kVA single-phase H-bridge, LCL filter, local load, STS, weak tie
I	Van der Pol core	Oscillator synthesised from the voltage window; $\alpha = 2/3\,\sigma$ fixes V_{oc}=κ_v
I	Amplitude retune	σ scaled by 1.15 to stiffen the amplitude loop without moving V_{oc}
I	Secondary layer	Voltage PI on κ_v, frequency integrator on C, islanded only
I	Synchronisation	Phase PI acting on C; STS latch on 2% voltage, 0.05 rad, 0.75 s hold
I	Tertiary redesign	Dispatch gains re-derived from the characteristic equation; dominant time constant 0.738 s → 0.117 s
II	AHO background	VI-AHO inertia and feedforward damping studied before implementation
II	IAHO core	AHO in $\alpha\beta$, SOGI-QSG quadrature, resonant inertia path
II	Secondary re-anchoring	Secondary loops moved to act directly on V_{p0} and ω^* with positive gains, replacing the VOC-style action on C
II	Damping synthesis	$G_p(s)$, $G_\omega(s)$ recomputed at run time from K_s, T_i, T_{so}, ζ, ω_n
II	Bandwidth study	ω_{n1} swept over 2π–6π; 3π selected
II	Volt-var disabled	Grid-tied volt-var PI removed from the IAHO build to keep it faithful to the published controller

Phase	Step	Outcome
II	Current limiting	IAHO virtual-impedance limiter finalised at 1.20 pu peak-current basis; threshold sensitivity produced no noticeable waveform change, while limiter status was not exported.
III	Matching	Plant, tie, load, references, event magnitudes and instants aligned
III	Final comparison	Six disturbances, metrics extracted from exported CSV data

3.2 Single-phase inverter model

Figure 2(a) shows the common power circuit; Figure 2(b) is the PLECS implementation both controllers share.

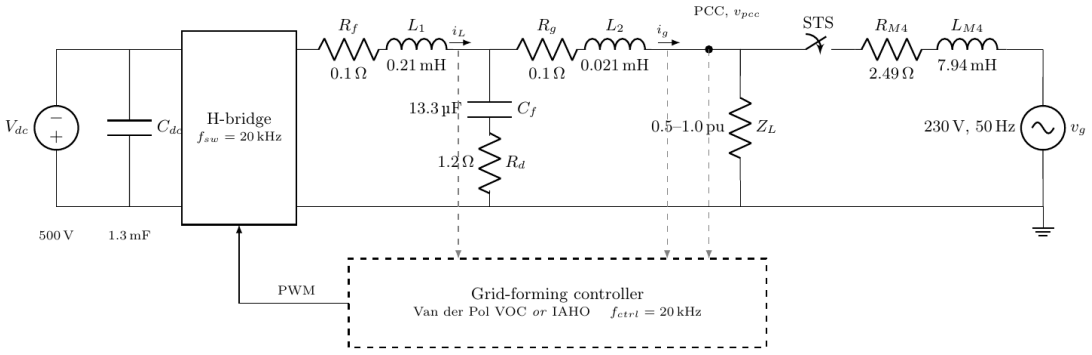


Figure 2(a) Simplified single-phase 10 kVA grid-forming inverter: power stage, LCL filter, local load, STS and weak-grid connection, common to both controller implementations.

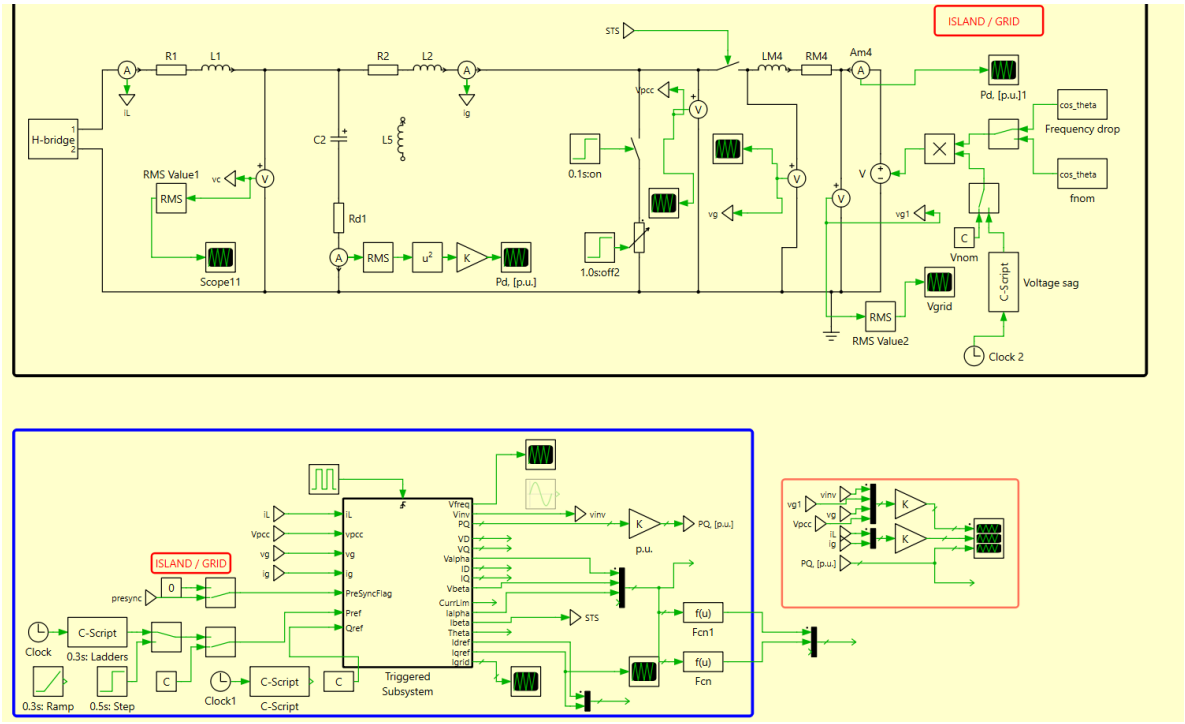


Figure 2(b) PLECS implementation of the same inverter: LCL filter, PCC measurement, STS, weak-grid tie, disturbance blocks and the controller interface used in every simulation.

A 500 V DC source feeds a 20 kHz H-bridge through a 1.3 mF DC link. The LCL filter uses L_1 = 0.21 mH, C_f = 13.3 µF with R_d = 1.2 Ω, and L_2 = 0.021 mH, with 0.1 Ω of parasitic resistance in each inductor. Filter resonance lands at roughly 9.99 kHz.

The PCC sits downstream of L_2, immediately ahead of the STS. The capacitor voltage v_c is measured upstream of L_2, so v_c and v_{pcc} are not the same signal. The local resistive load is connected at the PCC, and the STS connects this node to the grid through the tie impedance.

Every reported test uses L_{M4} = 7.94 mH and R_{M4} = 2.49 Ω. With the filter parasitics included this becomes R_T = 2.69 Ω and X_T = 2.57 Ω, hence R_T/X_T = 1.05 and SCR ≈ 1.4, which is a deliberately weak and resistive connection.

Using the same single-phase RMS base throughout the report, the short-circuit ratio is defined from the Thevenin impedance seen at the PCC as

$$\mathrm{SCR} = \mathrm{Ssc} / \mathrm{Sn}, \quad \mathrm{Ssc} = \mathrm{Vn}^2 / |\mathrm{Zth}|, \quad |\mathrm{Zth}| = \sqrt{(\mathrm{RT}^2 + \mathrm{XT}^2)}.$$

With Vn = 230 V, RT = 2.69 Ω and XT = 2.57 Ω, Ssc ≈ 14.2 kVA and SCR ≈ 1.42 (reported as 1.4).

The measured signals are v_{inv}, v_{pcc}, inverter-side current i_L and grid-side current i_g. Active and reactive power are computed from v_{pcc} and i_g and then filtered at $\omega_c = 2\pi(20)$ rad/s.

One implementation asymmetry should be noted. IAHO takes its primary feedback from i_L, the Van der Pol oscillator from i_g. Comparisons of delivered current therefore use i_g, while inverter loading is read from i_L. Section 3.14 retains this difference explicitly in the comparison.

The common plant and network parameters are collected in Table 2.

Table 2 Inverter and network parameters, identical in both models.

Parameter	Symbol	Value	Basis
Rated apparent power	S_n	10 kVA	System rating
Nominal RMS voltage	V^*	230 V	System rating
Nominal frequency	f_n	50 Hz	Grid standard
DC-link voltage	V_{dc}	500 V	Inverter design
DC-link capacitance	C_{dc}	1.3 mF	Common plant
Switching frequency	f_{sw}	20 kHz	Common plant
Control frequency	f_{ctrl}	20 kHz	Common plant
Inverter-side inductor	L_1	0.21 mH	Common plant
Filter capacitor	C_f	13.3 µF	Common plant
Capacitor damping	R_d	1.2 Ω	Common plant
Grid-side inductor	L_2	0.021 mH	Common plant
Tie inductance	L_{M4}	7.94 mH	Matched test condition
Tie resistance	R_{M4}	2.49 Ω	Matched test condition
Total path reactance	X_T	2.57 Ω	Derived
Total path resistance	R_T	2.69 Ω	Derived
Rated peak current	I_{rated}	61.49 A	$\sqrt{2}S_n/V^*$

Parameter	Symbol	Value	Basis
Power-filter bandwidth	ω_c	$2\pi(20)$ rad/s	Common measurement

Both controller blocks see the same plant and the same sensor signals; only the primary current-feedback point differs. The electrical plant itself is identical.

3.3 Single-phase SOGI-based quadrature signal generation

A single-phase system offers one physical voltage waveform and one current waveform, so the orthogonal components a controller needs are not there to be measured and must be constructed. Single-phase instantaneous power also carries an inherent double-frequency component. For sinusoidal voltage and current,

$$p(t) = v(t)i(t) = VI\cos\phi + VI\cos(2\omega t - \phi)$$

$$p(t) = P + VI\,cos(2\omega t - \phi)$$

In a 50 Hz system, then, the power signal carries a 100 Hz ripple, and the fundamental has to be extracted and filtered before any slower control function uses it.

Both implementations lean on SOGI-based processing, but not for the same reason. In the Van der Pol model the SOGI blocks serve measurement, power calculation and synchronisation. The IAHO needs one more: a dedicated SOGI quadrature signal generator (SOGI-QSG) sitting in the primary current-feedback path. For a measured current its transfer functions are [14]

$$G_\alpha(s) = \frac{i_\alpha(s)}{i(s)} = \frac{K_{so}\omega s}{s^2+K_{so}\omega s+\omega^2}\; G_\beta(s) = \frac{i_\beta(s)}{i(s)} = \frac{K_{so}\omega^2}{s^2+K_{so}\omega s+\omega^2} \tag{1}$$

The two outputs are an in-phase α component and a 90°-shifted β component.

$$\frac{\bar{I}_{\alpha\beta}(s)}{\bar{I}(s)} = \frac{1}{T_{so}s+1},\; T_{so} = \frac{2}{K_{so}\omega_0} \tag{2}$$

With $K_{so} = 0.707$ at 50 Hz ($\omega_0 = 2\pi \times 50$ rad/s), $T_{so} = \frac{2}{0.707\times 2\pi\times 50} \approx 9.0$ ms

That lag is carried through into the IAHO (Integrated Andronov–Hopf Oscillator) inertia and damping model; this lag is not present in the primary Van der Pol oscillator dynamics.

3.4 Van der Pol VOC

The hierarchical Van der Pol VOC used as the Phase I reference is shown in Figure 3.

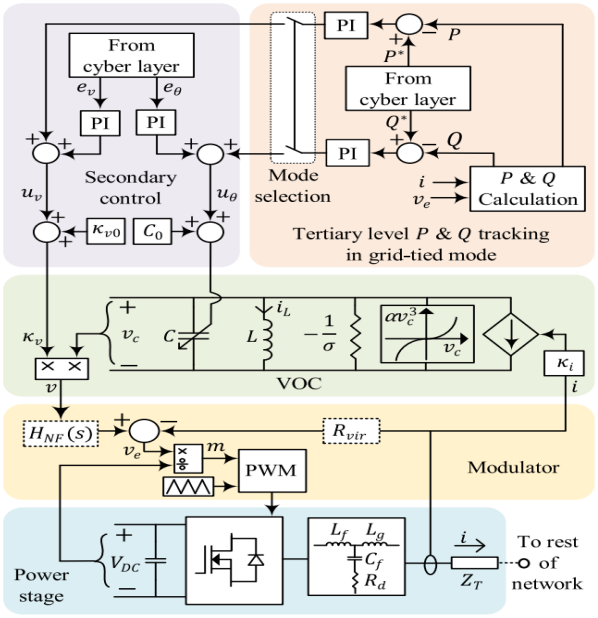


Figure 3 Reference hierarchical Van der Pol VOC architecture [4]. The implementation here follows the same core control structure, but the third-harmonic notch filter and virtual resistance of the reference are left out of the final Van der Pol model.

At the core sits a Van der Pol virtual RLC oscillator with nonlinear conductance and measured-current feedback [4]:

$$L\frac{\mathrm{d}i_{Lv}}{\mathrm{d}t}=\frac{v}{\kappa_v},\qquad C\frac{\mathrm{d}v}{\mathrm{d}t}=\underbrace{-\alpha\frac{v^3}{\kappa_v^2}}_{\text{dissipating}}+\underbrace{\sigma v}_{\text{energising}}-\kappa_v i_{Lv}-\kappa_v\kappa_i\, i, \qquad (3)$$

Here v is the oscillator voltage reference, i_{Lv} the virtual tank current, κ_v and κ_i scaling gains, and σ and α set the nonlinear conductance.

At small amplitude the linear term pumps energy in; at large amplitude the cubic term takes it out, and the balance between the two is the stable limit cycle. One consequence matters for black start: because the cubic acts on instantaneous voltage, amplitude and phase stay coupled during large excursions.

Averaged over one fundamental cycle, the amplitude and phase dynamics are

$$v(t):=\sqrt{2}\,V(t)\cos\{\varphi(t)\}, \qquad (4)$$

where V is the cycle-averaged RMS voltage and φ the oscillator phase.

$$\frac{\mathrm{d}V}{\mathrm{d}t}=\frac{\sigma}{2C}\left[V-\frac{\beta}{2}V^3\right]-\frac{\kappa_v\kappa_i}{2CV}P, \qquad (5)$$

$$\frac{\mathrm{d}\varphi}{\mathrm{d}t}=\omega^*+\frac{\kappa_v\kappa_i}{2CV^2}Q,\qquad \beta=\frac{3\alpha}{\kappa_v^2\sigma}. \qquad (6)$$

What matters structurally is the channel pairing that falls out of this: active power drives voltage amplitude and reactive power drives phase and frequency, i.e. P→V and Q→ω. The IAHO does the opposite, and much of the comparison later traces back to that single point.

At equilibrium the averaged model yields the droop relations

$$V_{eq} = V_{oc} + m_P P_{eq}, \qquad \omega_{eq} = \omega^* + m_Q Q_{eq}, \qquad (7)$$

whose no-load values and slopes are

$$V_{oc} = \kappa_v \sqrt{\frac{2\sigma}{3\alpha}}, \qquad \omega^* = \frac{1}{\sqrt{LC}}, \qquad (8)$$

$$m_P = \frac{\kappa_v \kappa_i}{2\sigma}\left[V_{eq} - \frac{3\alpha}{\kappa_v^2 \sigma} V_{eq}^3\right]^{-1}, \qquad m_Q = \frac{\kappa_v \kappa_i}{2CV_{eq}^2}. \qquad (9)$$

Local asymptotic stability holds while $0 \le P_{eq} < P_{crit}$, where

$$P_{crit} = \frac{\sigma^2 \kappa_v}{6\alpha\kappa_i}. \qquad (10)$$

Equations (8)–(10) are used in Section 3.5 to determine κv, κi, σ, α, C and L from the specified voltage window and permitted frequency deviation.

Around the primary oscillator sit islanded secondary voltage and frequency control, pre-synchronisation, grid-tied P/Q tracking, volt-var support, an outer P–f support loop and the STS logic. None of these belong to the Van der Pol oscillator itself, and they are treated as additions throughout.

Two features of [4] are not implemented here: the third-harmonic notch filter HNF(s) and the virtual resistance Rvir. The oscillator therefore runs with its native harmonic content, which Section 4.10 quantifies.

3.5 Van der Pol parameter selection

Tuning of the Van der Pol controller came before any IAHO comparison and used the averaged relations above. The five steps are set out below; the numbers quoted are those of the final model.

Step 1 — voltage window. No-load and rated-load targets set a ±5% band around 230 V.

$$V_{oc} = 1.05V^* = 241.5 \qquad V_{min} = 0.95V^* = 218.5$$

Step 2 — fixing α against σ. From (8), choosing

$$\alpha = 2/3\,\sigma \quad \Rightarrow \quad V_{oc} = \kappa_v \sqrt{\frac{2\sigma}{3 \cdot \frac{2}{3}\sigma}} = \kappa_v \qquad (11)$$

This gives $\kappa_v = V_{oc} = 241.5$ V/V and $\kappa_i = V_{min}/P_{rated} = 0.02185$ A/W. Scaling σ and α together after that changes amplitude stiffness while leaving the no-load voltage where it is.

Step 3 — the nonlinear conductance. The synthesis relation of [6] then gives, from the voltage window,

$$\sigma_{design} = \frac{V_{oc}}{V_{min}} \cdot \frac{V_{oc}^2}{V_{oc}^2 - V_{min}^2} = 6.093. \qquad (12)$$

The value actually implemented, σ = 7.007, is $1.15\sigma_{\text{design}}$, with α = 4.671. That empirical PLECS retune stiffens the amplitude loop without moving V_{oc}.

That leaves a stability limit of P_{crit} = 1.94 pu, comfortably above every operating point tested.

Step 4 — virtual capacitance. Two bounds apply here, one from frequency droop and one from third-harmonic content, and C is taken from whichever is larger.

The frequency-droop bound asks that reactive loading to rated Q move frequency by no more than $\Delta\omega_{\text{max}}$:

$$m_Q Q_{rated} = \frac{\kappa_v \kappa_i Q_{rated}}{2CV_{min}^2} \leq \Delta\omega_{max} \;\Rightarrow\; C \geq \frac{\kappa_v \kappa_i Q_{rated}}{2V_{min}^2 \Delta\omega_{max}}. \qquad (13)$$

With the scaling already selected, this gives

$$C \geq \frac{1}{2\Delta\omega_{max}} \cdot \frac{V_{oc}}{V_{min}} \cdot \frac{Q_{rated}}{P_{rated}} = 0.1759 \text{ F}, \qquad (14)$$

taking $\Delta\omega_{\text{max}} = 2\pi(0.5)$ rad/s at rated reactive power.

$$\omega^* = 1/\sqrt{(LC)}, \quad L = 1/(\omega^{*2}C), \quad \varepsilon = \sqrt{(L/C)} = 1/(\omega^* C).$$

Separately, the cubic nonlinearity imposes its own third-harmonic bound

$$\delta_{31} = \frac{\sigma}{8\omega^* C} \;\Rightarrow\; C \geq \frac{\sigma_{design}}{8\omega^* \delta_{31}} = 0.1212 \text{ F} \qquad (15)$$

$$L = 1/(\omega^{*2}C) = 57.6\ \mu\text{H}, \quad \varepsilon = \sqrt{(L/C)} = 0.0181.$$

For δ_{31} = 2% the frequency-droop bound is the binding one, so C = 0.1759 F and L = 57.6 μH.

The implemented parameters predict δ_{31} = 1.59%, against a measured 1.449%, so the prediction holds to within 9%.

$$K_{p,Q} = 1.5 \times 10^{-7} K_{i,Q} = 1.0 \times 10^{-6}$$

Secondary, synchronisation and reactive-power gains were tuned in PLECS, and the final values appear in Table 5. Grid support uses a 2% outer P–f characteristic with a 0.02 Hz deadband, plus a volt-var PI capped at 7 kVAr.

3.6 Grid pre-synchronisation and static transfer switch logic

Both models follow the same sequence: islanded operation, pre-synchronisation, then STS closure. Grid and PCC PLLs supply the phase error while pre-synchronising, and one-cycle RMS blocks supply the voltage-magnitude error:

$$\Delta V = V_{g,RMS} - V_{PCC,RMS}, \quad e_\theta = \theta_{g,PLL} - \theta_{PCC,PLL} \qquad (17)$$

The two phase controllers are

Van der Pol:

$$u_{\text{sync}} = -K_{p,\phi} e_\theta - K_{i,\phi} \int e_\theta \, dt, \; C_{\text{cmd}} = C_0 + u_{\text{sync}}$$

IAHO:

$$\omega'_{0,\text{sync}} = \omega_{g,\text{PLL}} + K_{\text{sync}}\sin(e_\theta) + u_I,\ \frac{du_I}{dt} = K_{i,\text{sync}}\sin(e_\theta),\ K_{i,\text{sync}} = 0.25K_{\text{sync}}^2 \quad (18)$$

The Van der Pol loop moves frequency indirectly, through C, while the IAHO acts on its centre frequency directly and adds an integral phase trim. The final IAHO uses Ksync = 20 (rad/s)/rad.

Closure criteria are identical in both models. The STS closes only when

$$|\Delta V| \le 0.02\,V^* \quad \text{and} \quad |\Delta\theta| \le 0.05 \text{ rad, held for } T_{hold} = 0.75 \text{ s}, \quad (19)$$

The closure criteria must hold continuously for T_hold = 0.75 s, so any difference in closure time reflects controller convergence rather than a difference in latching logic.

Both models seed their states at closure to keep the transition bumpless. The IAHO also blends its grid-connected reference in over 0.30 s, so the inertial path is not bypassed at the moment of connection.

Neither primary oscillator needs a PLL to stay synchronised once connected. The PLLs are there for pre-synchronisation and readout. Beyond that, the Van der Pol outer P–f support draws on filtered grid-PLL frequency, while the IAHO damping path uses the SOGI-FLL of Section 3.10.

3.7 Andronov–Hopf oscillators and virtual inertia

Conventional AHO. The AHO is an $\alpha\beta$ nonlinear oscillator built around a norm-based restoring term. Amplitude and phase dynamics separate cleanly and the voltage it produces is autonomous and sinusoidal, but the basic P–f response is first order, which means no virtual inertia.

Subsequent developments in AHO control. Luo et al. [10] introduced a resonant controller in the current-feedback path; its averaged first-order lag supplies virtual inertia and reduces RoCoF. The additional dynamic order can, however, reduce damping and increase overshoot.

Rezazadeh et al. [11] addressed this with feedforward damping driven by Pref and the estimated grid frequency, which keeps the inertial path intact while reshaping the active-power response for the single-phase case.

IAHO. The integrated controller [1] combines three functions:

- virtual inertia from the resonant current path;
- feedforward damping enhancement to suppress the oscillation introduced by the inertial lag;
- voltage-independent active-power droop so frequency support does not weaken during a voltage sag.

Inertia comes from the resonant current-error controller

$$\mathbf{y}'_{\alpha\beta} = G_R(s)\left(\mathbf{i}_{\alpha\beta,ref} - \mathbf{i}_{\alpha\beta}\right), \quad (20)$$

whose averaged magnitude is the first-order lag

$$\frac{Y'(s)}{I_{er}(s)} = \frac{\omega_f}{s+\omega_f} = \frac{1}{T_f s + 1}, \qquad T_f = \frac{1}{\omega_f}. \quad (21)$$

The time constant T_f slows the frequency response to a power mismatch, and that delay is what the inverter presents as inertia.

For a step power mismatch, the initial frequency rate is

$$\left.\frac{d\omega}{dt}\right|_{t=0^+} = \frac{\eta\,\Delta P}{T_f}. \qquad (22)$$

Using $\eta S_n = R_{droop}\omega_0$, the RoCoF design becomes

$$\mathrm{RoCoF}_{max} = \frac{1}{2\pi}\cdot\frac{\eta S_n}{T_f} = \frac{R_{droop} f_n}{T_f} \quad \Rightarrow \quad T_f = \frac{R_{droop} f_n}{\mathrm{RoCoF}_{max}}. \qquad (23)$$

For 2% droop and a 36 Hz/s design budget this gives $T_f = 27.8$ ms and $\omega_f = 36$ rad/s.

Comparing with the synchronous-machine swing equation in per unit gives

$$\frac{d\omega_{pu}}{dt} = \frac{R_{droop}}{T_f}\Delta P_{pu}. \qquad (24)$$

$$H_{eq} = \frac{T_f}{2R_{droop}} = 0.694 \text{ s}. \qquad (25)$$

This corresponds to a substantially smaller inertial time constant than the source paper uses (Tf = 159 ms). A second implication is that Tso = 9.0 ms cannot be neglected here: Tf ≈ 3.1Tso, so the SOGI dynamics must remain in the single-phase model.

Damping is then recovered through the feedforward design of Section 3.9, without giving up this inertial path.

3.8 IAHO controller

Phase II followed the published IAHO architecture of Figure 4.

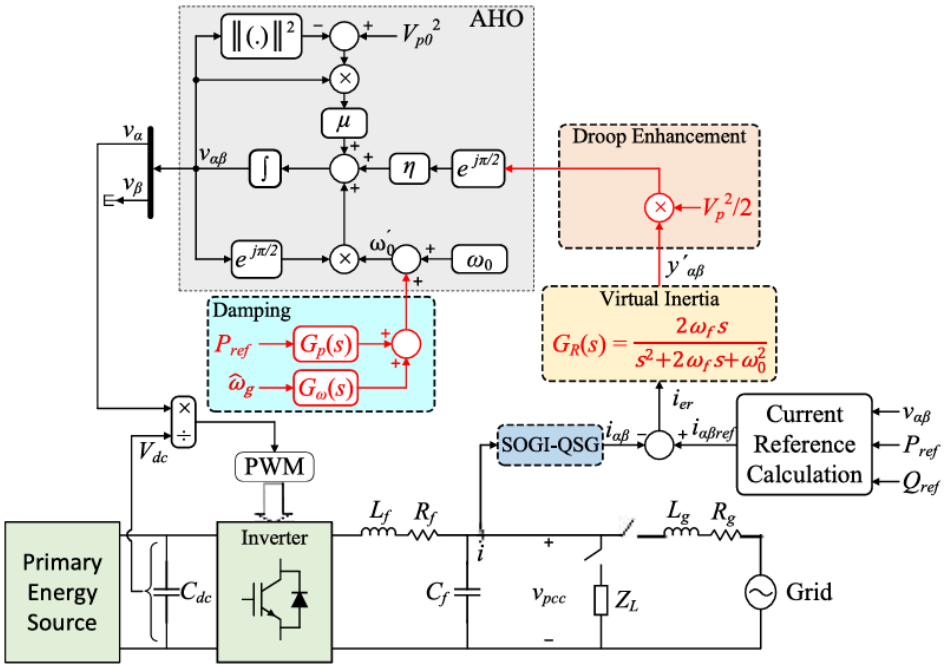


Figure 4 Reference Integrated Andronov-Hopf Oscillator (IAHO) architecture [1]. The implementation here keeps this core structure and adds the synchronisation, secondary-voltage and current-protection functions of Sections 3.6, 3.11 and 3.12.

In the $\alpha\beta$ frame the AHO core is [1]:

$$\begin{bmatrix}\dot{v}_\alpha \\ \dot{v}_\beta\end{bmatrix} = \begin{bmatrix}\mu\left(V_{p0}^2 - V_p^2\right) & -\omega_0{}' \\ \omega_0{}' & \mu\left(V_{p0}^2 - V_p^2\right)\end{bmatrix}\begin{bmatrix}v_\alpha \\ v_\beta\end{bmatrix}, \qquad V_p = \sqrt{v_\alpha^2 + v_\beta^2}, \qquad (26)$$

$$\theta = \arctan\left(v_\beta / v_\alpha\right)$$

where V_{p0} is the nominal voltage magnitude and μ sets how fast the amplitude converges. In polar coordinates, amplitude and phase separate:

$$\dot{V}_p = \mu\left(V_{p0}^2 - V_p^2\right)V_p, \qquad \dot{\theta} = \omega_0{}'. \qquad (27)$$

$$\| \mathbf{v} \| = V_p$$

Since the restoring term depends only on the norm of the state vector, the AHO is isotropic, and the Van der Pol cubic third-harmonic mechanism has no counterpart here.

Current feedback is applied through the virtual-inertia output $y'\alpha\beta$, giving

$$\begin{aligned}\dot{v}_\alpha &= \mu\left(V_{p0}^2 - V_p^2\right)v_\alpha - \omega_0{}' v_\beta - \frac{\eta V_p^2}{2} y'_\beta, \\ \dot{v}_\beta &= \omega_0{}' v_\alpha + \mu\left(V_{p0}^2 - V_p^2\right)v_\beta + \frac{\eta V_p^2}{2} y'_\alpha,\end{aligned} \qquad (28)$$

Averaging the resonant and SOGI dynamics leaves the working IAHO model:

$$\dot{V}_p = \mu\left(V_{p0}^2 - V_p^2\right)V_p + \eta V_p \frac{1}{T_f s + 1}\left(Q_{ref} - \frac{1}{T_{so} s + 1} Q\right), \qquad (29)$$

$$\dot{\theta} = \omega = \omega_0{}' + \eta \frac{1}{T_f s + 1}\left(P_{ref} - \frac{1}{T_{so} s + 1} P\right). \qquad (30)$$

The channel assignment is machine-like: P drives phase and frequency, Q drives voltage amplitude. An islanded active-power step therefore shows up as a deliberate frequency transient rather than mostly as a voltage transient.

Because η multiplies the active-power mismatch directly, the P–f coefficient does not depend on V_p and stays consistent through a voltage sag.

3.9 Feedforward damping controller synthesis

For damping synthesis the inverter and grid are represented by the total tie impedance R_T + jX_T, giving the source-paper linearised power relation [1]

$$P \approx \frac{V_p V_g}{2X_T}\,\delta = K_s\,\delta, \qquad Q \approx \frac{V_p}{2X_T}\left(V_p - V_g\right), \qquad (31)$$

where δ = θ − θg and Ks = 20 608 W/rad for this system. Because the tested tie is strongly resistive (RT/XT = 1.05), this inductive-grid power-angle relation is retained only as a controller-synthesis approximation consistent with the IAHO design method. The resulting coefficients are verified against the complete R–X switching model in PLECS rather than treated as an exact description of the plant.

With virtual inertia, the active-power loop becomes third order. The corrected centre frequency is

$$\omega_0{}' = \omega_0 + G_p(s)P_{ref} + G_\omega(s)\hat{\omega}_g, \qquad (32)$$

The corresponding closed-loop active-power responses are:

$$\frac{\Delta P(s)}{\Delta P_{ref}(s)} = \frac{DK_s + G_p(s)(T_f s + 1)K_s}{T_{so}T_f s^3 + (T_f + T_{so})s^2 + s + DK_s}, \quad (33)$$

$$\frac{\Delta P(s)}{\Delta \omega_g(s)} = \frac{(G_{FLL}(s)G_\omega(s) - 1)(T_f s + 1)K_s}{T_{so}T_f s^3 + (T_f + T_{so})s^2 + s + DK_s}, \quad (34)$$

Without $G_p(s)$ and $G_\omega(s)$ this inertial loop can end up lightly damped, so the desired responses are specified as second-order targets

$$\frac{\Delta P(s)}{\Delta P_{ref}(s)} = \frac{\omega_{n1}^2}{s^2 + 2\zeta\omega_{n1}s + \omega_{n1}^2}, \qquad \frac{\Delta P(s)}{\Delta \omega_g(s)} = -\frac{1}{D}\frac{\omega_{n2}^2}{s^2 + 2\zeta\omega_{n2}s + \omega_{n2}^2}, \quad (35)$$

Solving for the two feedforward controllers gives

$$G_p(s) = \frac{b_1' s^2 + c_1 s}{d_1 s^3 + e_1 s^2 + f_1 s + g_1}, \qquad G_\omega(s) = \frac{a_2 s^3 + b_2 s^2 + c_2 s}{d_2 s^3 + e_2 s^2 + f_2 s + g_2}, \quad (36)$$

where the coefficients, for i = 1,2, are

$$a_1 = \omega_{n1}^2 T_{so} T_f, \qquad b_1 = \omega_{n1}^2 (T_f + T_{so}) - DK_s,$$

$$c_1 = \omega_{n1}^2 - 2\zeta\omega_{n1} DK_s, \qquad b_1' = \frac{1}{2}\left(b_1 - \sqrt{b_1^2 - 4a_1 c_1}\right),$$

$$a_2 = -\frac{\omega_{n2}^2 T_{so} T_f}{D} + K_s T_f,$$

$$b_2 = -\frac{\omega_{n2}^2 (T_f + T_{so})}{D} + K_s(1 + 2\zeta\omega_{n2} T_f),$$

$$c_2 = -\frac{\omega_{n2}^2}{D} + K_s(T_f \omega_{n2}^2 + 2\zeta\omega_{n2}), \qquad d_i = K_s T_f,$$

$$e_i = K_s(1 + 2\zeta\omega_{ni} T_f), \qquad f_i = K_s(T_f \omega_{ni}^2 + 2\zeta\omega_{ni}), \qquad g_i = K_s \omega_{ni}^2. \quad (37)$$

For $i = 1$, $\zeta_i = \zeta_P$ and $\omega_{ni} = \omega_{n1}$; for $i = 2$, $\zeta_i = \zeta_F$ and $\omega_{ni} = \omega_{n2}$.

The remaining tuning objectives are damping and bandwidth: ζ governs overshoot, ωn1 sets the active-power dispatch bandwidth, and ωn2 sets the response bandwidth to grid-frequency changes.

The final implementation uses $\zeta_P = 1.00$, $\zeta_F = 1.15$, $\omega_{n1} = 3\pi$ rad/s and $\omega_{n2} = 6\pi$ rad/s. These four were chosen in PLECS for a fast, strongly damped response rather than copied from the paper.

Coefficients are recomputed at the start of each simulation from K_s, T_f and T_{so}, which keeps the damping design tied to the network actually simulated.

3.10 SOGI-FLL-based grid-frequency estimation

The IAHO frequency-disturbance feedforward path $G_\omega(s)$ needs an estimate of grid frequency to work with, and a SOGI-FLL supplies $\hat{\omega}_g$ from the measured grid voltage [15]:

$$G_{FLL}(s) = \frac{\Delta\hat{\omega}_g(s)}{\Delta\omega_g(s)} = \frac{\omega_{n\text{-}FLL}^2}{s^2 + 2\xi_{FLL}\omega_{n\text{-}FLL}s + \omega_{n\text{-}FLL}^2}, \quad (38)$$

$$K_{i\text{-}FLL} = 2\omega_{n\text{-}FLL}^2, \qquad K_{p\text{-}FLL} = \frac{4\xi_{FLL}\omega_{n\text{-}FLL}}{\omega_0}. \qquad (39)$$

The implementation uses $\xi_{FLL} = 0.9$ and $\omega_{n\text{-}FLL} = 150$ rad/s, a compromise between tracking speed and noise sensitivity.

Separate grid and PCC PLLs are kept for pre-synchronisation and readout. The frequency signals used by the two controllers differ: Van der Pol outer P–f support uses filtered grid-PLL frequency, while the IAHO damping term $G_\omega(s)$ uses the SOGI-FLL estimate.

3.11 IAHO reactive-power–voltage droop and voltage support

At steady state the IAHO amplitude equation fixes how voltage answers a reactive-power mismatch:

$$0 = \mu\left(V_{p0}^2 - V_p^2\right)V_p + \eta V_p\left(Q_{ref} - Q\right). \qquad (40)$$

Linearising around $V_p = V_{p0}$ gives the Q–V droop slope

$$m_q = \left|\frac{\Delta V}{\Delta Q}\right| = \frac{\eta}{2\mu V_{p0}} \quad \Rightarrow \quad \mu = \frac{\eta}{2m_q V_{p0}}. \qquad (41)$$

This is the relation that sets μ. A 4% amplitude droop at $Q_0 = 0.6S_n$ was specified, giving $m_q = 2.169\times10^{-3}$ V/VAr and $\mu = 4.454\times10^{-4}$.

During a sag the Q mismatch increases the oscillator amplitude, which drives reactive support. The IAHO volt-var PI is switched off in grid-connected mode, so the intrinsic Q–V droop provides the reactive support without an additional volt-var loop.

The secondary voltage PI is active only in islanded and pre-synchronisation operation, and it fades out once the STS closes.

3.12 Current limiting via virtual impedance

Both models protect against over-current, although the protection structures are not identical. The final IAHO activates a virtual-impedance limiter at 1.20 pu of the fundamental inverter-current vector magnitude on a rated-peak-current basis; the Van der Pol model retains its native current-protection path at 1.50 pu.

For the IAHO, current above the threshold generates virtual resistance and reactance according to

$$R_v = K_{rv}\frac{|i| - I_{th}}{I_{rated}}, \qquad X_v = K_{xv}\frac{|i| - I_{th}}{I_{rated}}, \qquad (42)$$

with $K_{rv} = 0.1$ and $K_{xv} = 3.0\ \Omega$ per pu of excess. The correction is applied to the voltage command, not to the oscillator states.

Both the virtual impedance and the voltage correction are capped, and the common $0.98\,V_{dc}$ modulation clamp applies after that.

Moving the IAHO threshold from 0.8 pu to 1.20 pu produced no noticeable change in the reported disturbance waveforms. Because the limiter-activation signal was not exported, its instantaneous contribution cannot be isolated quantitatively. Current protection is therefore

retained as a documented implementation difference rather than treated as a demonstrated cause of the performance differences reported later.

3.13 IAHO parameter design and scaling

The published IAHO was validated on a 2.5 kVA single-phase converter, whereas the controller developed here is applied to a 10 kVA, 230 V inverter connected through a weaker and more resistive grid. The IAHO structure was therefore retained from the literature, but its numerical parameters were not copied directly. The final design used three parameter-selection routes: rating- or network-dependent quantities were recalculated analytically, dimensionless settings were retained from the literature where appropriate, and the remaining transient parameters were refined in the full PLECS switching model.

This distinction reflects the actual development process. The analytical relations defined the physical role and initial value of each parameter, while PLECS tuning was used where the complete inverter, SOGI dynamics, weak-grid impedance and synchronisation logic made the transient response more complicated than the reduced-order design model.

Step 1 — active-power droop gain η. The IAHO uses a machine-like P–f characteristic. At steady state,

$$\omega - \omega_0{}' = \eta(P_{ref} - P).$$

A 2% P–f droop was selected as the common overall frequency-support characteristic for the two controllers. At 50 Hz, a full-rated active-power mismatch therefore corresponds to a 1 Hz frequency deviation. For the 10 kVA base, the required IAHO droop gain is

$$\eta = \frac{R_{droop}\,\omega_0}{S_n} = 6.283 \times 10^{-4}\, rad/s/W.$$

Thus η is rating-dependent and was recalculated for the present inverter rather than transferred from the 2.5 kVA source system.

Step 2 — reactive-power droop and amplitude gain μ. The final model uses Q0 = 0.6Sn = 6 kVAr as its reactive-power design base and specifies a 4% voltage-amplitude change at that operating point. The corresponding Q–V slope is

$$m_q = \frac{\Delta V_{pu}\, V_{p0}}{Q_0} = 2.169 \times 10^{-3}\, V/VAr.$$

Linearising the IAHO amplitude equation about nominal voltage gives the relation between this droop slope and the oscillator amplitude gain. Hence

$$\mu = \frac{\eta}{2\, m_q\, V_{p0}} = 4.454 \times 10^{-4}.$$

The value of μ is therefore not an independent trial-and-error gain; once η, the selected Q–V droop and the reactive-power design base are fixed, μ follows from the analytical IAHO relation.

Step 3 — SOGI-QSG and frequency-estimator settings. The dimensionless SOGI-QSG gain Kso = 0.707 was retained from the single-phase AHO literature because it provides a practical

compromise between tracking bandwidth and noise sensitivity and does not require power-rating scaling. Its equivalent amplitude lag at 50 Hz is

$$T_{so} = \frac{2}{K_{so}\,\omega_0} = 9.0\,ms.$$

The SOGI-FLL settings ξFLL = 0.9 and ωn-FLL = 150 rad/s were likewise retained from the literature. These parameters determine estimator damping and bandwidth rather than converter power capability, so no 2.5-to-10 kVA scaling was required.

Step 4 — virtual-inertia setting. The resonant current-error path introduces the averaged lag 1/(Tfs + 1). The source design relation links the inertial time constant to droop and a selected RoCoF design target:

$$T_f = \frac{R_{droop}\,f_n}{RoCoF_{design}} = 27.8\,ms, \quad \omega_f = \frac{1}{T_f} = 36\,rad/s.$$

The 36 Hz/s quantity used in this calculation is an internal controller-design budget for the present simulation, not a grid-code RoCoF limit. The published IAHO design uses a much stricter 3.5 Hz/s criterion, which is retained in Table 3 only as a source-paper reference. Here, the analytical relation provided the starting point, and the smaller inertial time constant was retained after tuning the complete 10 kVA PLECS model. The final setting therefore prioritises the transient-speed requirements of this comparative simulation rather than reproducing the source paper's inertia constant. Its equivalent inertia constant is

$$H_{eq} = \frac{T_f}{2\,R_{droop}} = 0.694\,s.$$

This corresponds to a substantially smaller inertial time constant than the source-paper setting. Because Tso = 9.0 ms is no longer negligible relative to Tf = 27.8 ms, the SOGI lag is retained explicitly in the damping synthesis rather than ignored.

Step 5 — damping, bandwidth and synchronisation. The feedforward controllers Gp(s) and Gω(s) are designed to reshape the active-power dynamics toward a standard second-order target,

$$G_{target}(s) = \frac{{\omega_n}^2}{s^2 + 2\zeta\omega_n s + {\omega_n}^2}.$$

The damping ratio ζ controls ringing and overshoot, while the natural frequency ωn sets response speed. These parameters were refined in PLECS rather than copied from the paper because the final weak-grid plant has different rating, R/X ratio and measurement dynamics. The final values are

$$\zeta_P = 1.00, \quad \omega_{n1} = 3\pi\,rad/s; \quad \zeta_F = 1.15, \quad \omega_{n2} = 6\pi\,rad/s.$$

The selected ζP = 1.00 corresponds to a critically damped dispatch target, while ζF = 1.15 is mildly overdamped and suppresses oscillation in the grid-frequency channel. A direct PLECS sweep of ωn1 from 2π to 6π rad/s reduced the measured 90% dispatch time from 0.766 s to 0.493 s, but increased overshoot from 1.6% to 4.6%. The value 3π rad/s was therefore retained as the speed–overshoot compromise. The frequency-support channel was tuned more aggressively at 6π rad/s to obtain a faster response to grid-frequency changes.

The pre-synchronisation gain Ksync = 20 (rad/s)/rad was also selected in the full PLECS model. It gave sufficiently fast phase convergence without the excessive action that would result from applying a gain designed for an ideal, lag-free angle signal. Finally, the synchronising coefficient Ks and the coefficients of Gp(s) and Gω(s) are recomputed from the actual weak-grid tie and the selected dynamic targets at simulation start-up.

Table 3 summarises the final 10 kVA IAHO settings and distinguishes analytical scaling, literature values and PLECS-refined parameters.

Table 3 IAHO parameter selection for the 10 kVA implementation, alongside the corresponding source-paper values.

Quantity	Symbol	Value	Selection method	Paper
Droop percentage	R_{droop}	2%	Common comparison design choice	1%
Active-power droop gain	η	6.283×10^{-4} rad/s/W	Analytic from 2% P–f droop	—
Q–V droop slope	m_q	2.169×10^{-3} V/VAr	Analytic from 4% Q–V droop	—
Amplitude gain	μ	4.454×10^{-4}	Analytic from Q–V relation	2.38×10^{-4}
Q–V droop base	Q_0	6 kVAr	Reactive-power design base	—
Voltage droop at Q_0	ΔV_{pu}	4%	Q–V design choice	5%
SOGI gain	K_{so}	0.707	From literature	0.707
SOGI lag	T_{so}	9.0 ms	Derived from Kso	—
RoCoF budget	—	36 Hz/s	Internal simulation design target	3.5 Hz/s
Inertial time constant	T_f	27.8 ms	Analytic start; PLECS-refined	159 ms
Equivalent inertia	H_{eq}	0.69 s	Derived from Tf and droop	—
Synchronising coeff.	K_s	20 608 W/rad	Derived from actual tie	—
P_{ref} damping	ζ_P	1.00	PLECS damping tuning	0.85
ω_g damping	ζ_F	1.15	PLECS damping tuning	0.85
P_{ref} natural freq.	ω_{n1}	3π rad/s (1.5 Hz)	PLECS sensitivity sweep	2π
ω_g natural freq.	ω_{n2}	6π rad/s (3.0 Hz)	PLECS frequency-support tuning	4π
FLL damping	ξ_{FLL}	0.9	From literature	0.9
FLL natural freq.	$\omega_{n\text{-}FLL}$	150 rad/s	From literature	150

Quantity	Symbol	Value	Selection method	Paper
Pre-sync gain	K_{sync}	20 (rad/s)/rad	PLECS synchronisation tuning	—
Current threshold	I_{th}	1.20 pu (73.8 A pk)	Final IAHO protection setting; rated-peak-current basis	not present

The final IAHO design therefore combines three selection routes. η, μ, mq, Tso, Tf, Heq, Ks and the feedforward coefficients are obtained from analytical relations once the design targets are specified; Kso and the FLL settings are retained from the literature; and ζP, ζF, ωn1, ωn2 and Ksync are refined in PLECS against the complete 10 kVA switching model. This approach preserves the published IAHO structure while adapting its dynamic response to the actual converter rating and weak-grid network used in the comparison.

3.14 Matched-plant comparison methodology

The comparison is matched at the plant and disturbance level rather than by forcing the two controllers into identical architectures. The power stage, weak-grid tie, load, references, event magnitudes and event instants are identical. Controller-specific structures—such as feedback location, voltage/reactive-power support, frequency estimation and current protection—are retained because they are part of the implemented control laws and are stated explicitly below.

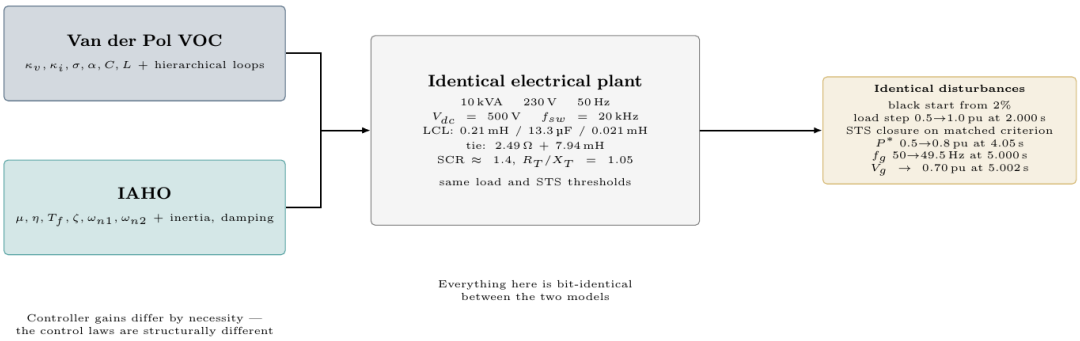


Figure 5 Matched comparison architecture. Plant, tie, load, references, event magnitudes and event instants are identical. The controller gains are not, and cannot be, since the two control laws are structurally different.

A fair comparison here means matching plant, ratings, references and disturbance conditions, rather than forcing structurally different controller gains to identical numerical values. Where differences remain, they are stated explicitly.

Table 4 lists the comparison conditions.

Table 4 Comparison conditions. External settings are matched; controller-specific items are listed separately.

Requirement	Setting	Basis
Rated power	10 kVA	Same
Rated voltage	230 V RMS	Same
Nominal frequency	50 Hz	Same

Requirement	Setting	Basis
DC voltage	500 V	Same
Switching frequency	20 kHz	Same
LCL filter	L_1, C_f, R_d, L_2	Same
Grid tie	7.94 mH, 2.49 Ω	Same
Local load	Signal-controlled resistor	Same
P–f droop	2%	Same
Q–V droop allowance	4–5% band	Comparable
Power filter	2π(20) rad/s	Same
Reference shaping	0.05 s	Same
STS voltage threshold	2% of 230 V	Same
STS phase threshold	0.05 rad	Same
STS hold time	0.75 s	Same
PLL tuning	2π(5) rad/s, ζ=0.707	Same
Load step	0.5 → 1.0 pu at t=2.0 s	Same
P^* step	0.5 → 0.8 pu at t=4.05 and 7.05 s	Same
Frequency step	50 → 49.5 Hz at t=5.0 s	Same
Voltage sag	0.70 pu at t=5.0 s	Same
Current protection	IAHO: 1.20 pu virtual impedance; VdP: native 1.50 pu protection	Documented difference

Four implementation differences remain:

1. The Van der Pol build carries a grid-connected volt-var PI with a 7 kVAr ceiling; the IAHO relies on intrinsic Q–V droop.
2. Van der Pol P–f support has a 0.02 Hz deadband; the IAHO has none.
3. Black-start initialisation differs slightly, and the IAHO adds a 50 ms amplitude soft-start ramp.
4. The primary feedback and protection interfaces differ: VdP uses i_g and its native 1.50 pu current-protection path, while IAHO uses i_L and a 1.20 pu virtual-impedance limiter. Raising the IAHO threshold from 0.8 to 1.20 pu changed no waveform noticeably.

The voltage-sag and black-start results are therefore read as comparisons of implemented configurations rather than of oscillator cores.

Table 5 collects the final controller settings.

Table 5 Final controller parameters for the matched Van der Pol VOC and IAHO comparison.

Controller	Parameter	Symbol	Value	Selection method	Main effect
VdP	Open-circuit voltage	V_{oc}	241.5 V	Design choice	No-load voltage
VdP	Voltage at rated power	V_{min}	218.5 V	Design choice	Droop depth
VdP	Voltage scaling	κ_v	241.5 V/V	Synthesis	Voltage reference scale
VdP	Current scaling	κ_i	0.02185 A/W	Synthesis	Droop slope
VdP	Negative conductance	σ	7.007	Synthesis, retuned	Amplitude stiffness
VdP	Cubic coefficient	α	4.671	$2/3\,\sigma$	Limit-cycle amplitude
VdP	Virtual capacitance	C	0.1759 F	Droop bound	Frequency deviation, δ_{31}
VdP	Virtual inductance	L	57.6 µH	$1/(C\omega_n^2)$	Oscillation frequency
VdP	Secondary voltage PI	$K_{p,v}, K_{i,v}$	0.2, 20	Tuned	Island voltage restoration
VdP	Secondary frequency	$K_{i,f}$	0.02	Tuned	Island frequency restoration
VdP	Tertiary P PI	$K_{p,P}, K_{i,P}$	1.133×10^{-4}, 0.015	Analytic	Dispatch tracking
VdP	Tertiary Q PI	$K_{p,Q}, K_{i,Q}$	1.5×10^{-7}, 10^{-6}	Tuned	Reactive tracking
VdP	Current threshold	Ilim,VdP	1.50 pu	Native protection setting	Over-current protection
VdP	Volt-var PI	k_{VQ}, k_{IV}	1700, 450	Tuned	Grid-tied voltage support
VdP	P–f droop	$K_{droop,f}$	10 kW/Hz	2% droop spec	Frequency support
IAHO	Droop gain	η	6.283×10^{-4}	Droop design	P–f response
IAHO	Amplitude gain	μ	4.454×10^{-4}	Voltage/Q design	Amplitude dynamics
IAHO	Inertial time constant	T_f	27.8 ms	RoCoF design	Virtual inertia
IAHO	SOGI lag	T_{so}	9.0 ms	K_{so} design	Measurement lag
IAHO	Dispatch damping	ζ_P	1.00	Damping design	Dispatch overshoot
IAHO	Grid-frequency damping	ζ_F	1.15	Damping design	Event overshoot

Controller	Parameter	Symbol	Value	Selection method	Main effect
IAHO	Dispatch bandwidth	ω_{n1}	3π rad/s	Tuned	Dispatch speed
IAHO	Grid-freq. bandwidth	ω_{n2}	6π rad/s	Tuned	Grid support speed
IAHO	Secondary voltage PI	$K_{p,v}, K_{i,v}$	$0.2\sqrt{2}$, $20\sqrt{2}$	Tuned	Island voltage restoration
IAHO	Secondary frequency	$K_{i,f}$	2.0	Tuned	Island frequency restoration
IAHO	Current threshold	I_{th}	1.20 pu	Final IAHO protection setting	Virtual-impedance activation

3.15 Disturbance scenarios

Solver settings and event timing are the same for every simulation. Each of the six tests runs once per controller, exporting the same signals: voltage, current, power, oscillator frequency and one-cycle RMS voltage.

Test 1 — islanded black start: no-load start from 2% oscillator amplitude.

Test 2 — islanded load step: resistive load 0.5→1.0 pu at t = 2.0 s.

Test 3 — pre-synchronisation and STS closure using Section 3.6.

Test 4 — grid-connected active-power step: P_{ref} 0.5→0.8 pu at 4.05 s and back at 7.05 s.

Test 5 — grid-frequency disturbance: 50→49.5 Hz at 5.0 s and recovery at 7.0 s. The applied source step has undefined RoCoF.

Test 6 — grid-voltage sag: source reduced to 0.70 pu for 3.0 s.

PCC-voltage harmonic analysis uses a separate steady-state record.

Only the weak tie of Section 3.2 (R_T/X_T = 1.05, SCR ≈ 1.4) is reported here.

3.16 Performance metrics and post-processing

The raw CSV files are large, so they are streamed into 0.2 ms bins holding minimum, maximum and mean values. Instantaneous peaks survive that, and the files stay manageable.

Voltage is reported as RMS, current on whichever peak or RMS base is appropriate, and power on S_n = 10 kVA. As a check, the logged PCC RMS signal was compared against a recomputed 20 ms sliding RMS; the two agreed to within 0.1–0.3 V.

Voltage and frequency extrema come from the one-cycle RMS and oscillator-frequency channels, and steady state is taken as the final 200 ms mean.

P and Q timing uses a centred 20 ms average, which removes the 100 Hz single-phase ripple without shifting the trace in time.

Rise time is the 10–90% transition. Settling bands are ±10 mHz for frequency, ±1.15 V for voltage and ±2% of the power step with a 50 W floor.

RoCoF. RoCoF is taken as a sliding least-squares slope of the oscillator frequency,

$$\mathrm{RoCoF}(t) = \left.\frac{\mathrm{d}f}{\mathrm{d}t}\right|_{\text{LS fit over } W}, \qquad W \in \{20,100,500\}\ \text{ms}. \qquad (44)$$

Every RoCoF value is quoted with the fitting window that produced it.

Peak $|i_g|$ is the true grid-side instantaneous peak; $I_{L,RMS}$ is the maximum 20 ms RMS inverter-side current. The two sit on different bases and are never compared directly.

Overshoot, undershoot, synchronisation time and damping ratio follow the same extraction rules for both controllers.

Limiter status and a few internal reference channels were never exported, so those signals cannot be reported directly.

4 Results

What follows is measured from the exported traces using the definitions of Section 3.16. Interpretation waits until Section 5.

One caveat carries through this section: current-protection status was not exported. The final IAHO uses a 1.20 pu virtual-impedance threshold and the Van der Pol model its native current-protection path, and the IAHO threshold sensitivity check showed no noticeable change in the reported waveforms.

4.1 Van der Pol baseline behaviour

The Van der Pol baseline starts on its own, holds nominal islanded voltage and frequency, and synchronises successfully before grid connection.

It settles at 229.96 V and 50.0000 Hz with no load and closes the STS at 1.850 s without loss of synchronism.

It also exposes the two limitations that motivated Phase II. Active load barely moves its frequency, a direct consequence of the P→V pairing, and grid-connected events excite a lightly damped 1.4–2.0 Hz mode.

4.2 Van der Pol design-relation study

Table 6 summarises the Van der Pol parameter study, built on the design relations of Section 3.5.

Table 6 Van der Pol parameter study. The effects listed are those predicted by the design relations of Section 3.5, checked against the implemented model.

Parameter	Primary effect	Too low	Too high	Selected	Basis
κ_v	Sets V_{oc} directly	Terminal voltage below nominal	Terminal voltage above nominal	241.5 V/V	$=V_{oc}$ via (11)
κ_i	Droop slope m_P	Poor load sharing	Deep voltage dip at rated load	0.02185 A/W	V_{min}/P_{rated}

Parameter	Primary effect	Too low	Too high	Selected	Basis
σ	Amplitude stiffness, pole σ/C	Slow voltage recovery, deeper dip	Larger third harmonic; approaches P_{crit}	7.007	$1.15\sigma_{design}$, retuned
α	Limit-cycle amplitude	V_{oc} rises	V_{oc} falls	4.671	$2/3\,\sigma$, holds V_{oc}
C	Frequency droop and δ_{31}	Frequency deviation exceeds target	Third harmonic exceeds 2% target	0.1759 F	Droop bound (14) binds
$K_{i,P}$	Dispatch speed	Slow reference tracking	Interacts with λ_A	0.015	Characteristic equation

Scaling σ and α by 1.15 stiffens the amplitude loop without moving V_{oc} and leaves P_{crit} = 1.94 pu. Re-deriving the tertiary gains pulls the dominant dispatch time constant from 0.738 s down to 0.117 s, still below the oscillator amplitude pole.

4.3 IAHO design-relation study

Table 7 does the same for the IAHO, drawing on the design relations of Sections 3.7–3.13 and the final PLECS sensitivity checks.

The principal rating-dependent relations are

$$\eta = \frac{R_{droop}\,\omega_0}{S_n} = 6.283 \times 10^{-4}\ rad/s/W$$

$$\mu = \frac{\eta}{2\,m_q\,V_{p0}} = 4.454 \times 10^{-4}$$

$$T_{so} = \frac{2}{K_{so}\,\omega_0} = 9.0\ ms$$

$$T_f = \frac{R_{droop}\,f_n}{RoCoF_{max}} = 27.8\ ms, \quad H_{eq} = \frac{T_f}{2\,R_{droop}} = 0.694\ s$$

Table 7 IAHO parameter study. The effects follow from the design relations of Sections 3.7–3.13 and from the final PLECS tuning study.

Parameter	Primary effect	Too low	Too high	Selected	Basis
η	P–f droop / frequency support	Weak active-power support	Large frequency response to power mismatch	6.283×10^{-4} rad/s/W	2% droop relation
μ	Amplitude stiffness / Q–V droop	Large voltage deviation; slow recovery	Very stiff voltage; reduced Q–V sensitivity	4.454×10^{-4}	Q–V relation (41)
K_{so}	SOGI bandwidth	Slow orthogonal-signal tracking	Greater noise / harmonic sensitivity	0.707	Literature; T_{so} = 9.0 ms

Parameter	Primary effect	Too low	Too high	Selected	Basis
T_f	Virtual inertia / RoCoF	Weak inertial effect; higher RoCoF	Slower inertial response; greater damping burden	27.8 ms	RoCoF relation (23)
ζ_P, ζ_F	Closed-loop damping	Ringing and overshoot	Slower overdamped response	1.00, 1.15	PLECS damping selection
ω_{n1}	Dispatch bandwidth	Slow active-power tracking	Higher overshoot	3π rad/s	PLECS sensitivity study
ω_{n2}	Grid-frequency support bandwidth	Slow frequency-support response	More aggressive transient response	6π rad/s	PLECS tuning

The ω_{n1} check produced the speed–overshoot trade-off one would expect: raising ω_{n1} from 2π to 6π rad/s cut the 90% dispatch time from 0.766 s to 0.493 s, but overshoot climbed from 1.6% to 4.6%. 3π rad/s was chosen as the compromise, with ζP = 1.00 and ζF = 1.15 keeping the response strongly damped.

A separate sensitivity check showed that reducing T_f from 159 ms to 50 ms changed the 90% dispatch time by only about 1 ms, confirming that $G_p(s)$ largely determines the shaped dispatch bandwidth.

4.4 Islanded black start

Both oscillators start from 2% amplitude into no load. Figure 6 gives the measured RMS and frequency response, Figure 7 the reconstructed fundamental PCC waveform.

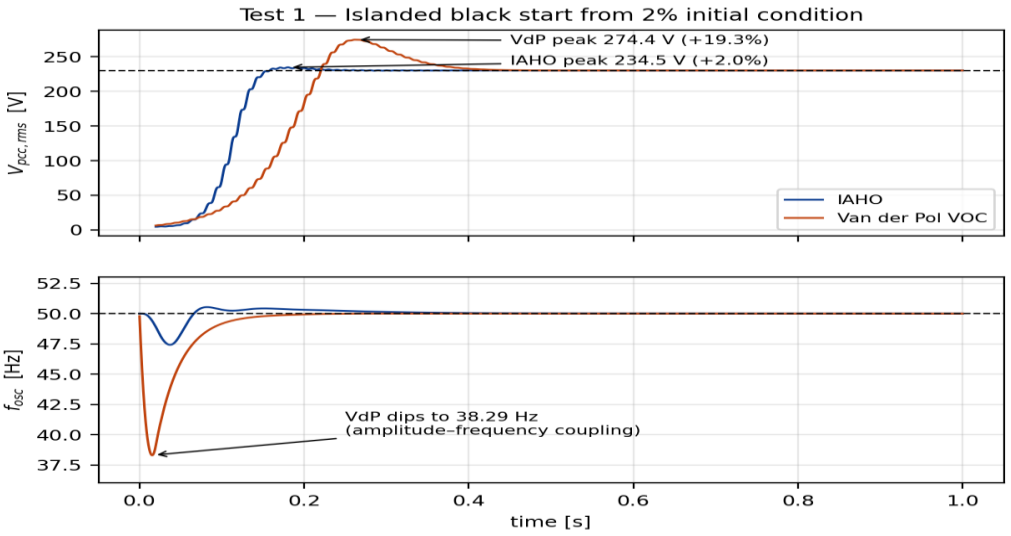


Figure 6 Islanded black start from 2% initial amplitude: measured PCC RMS voltage and oscillator frequency, IAHO against Van der Pol VOC.

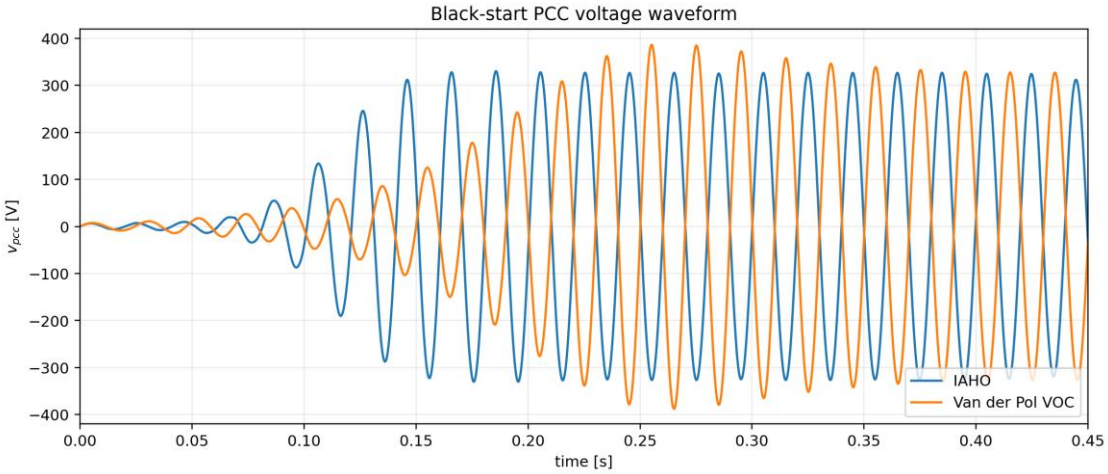


Figure 7 Black-start PCC voltage waveform, IAHO and Van der Pol VOC. The fundamental is reconstructed from the measured RMS-voltage envelope and the oscillator-frequency trace, so 20 kHz PWM switching ripple does not appear.

Table 8 Test 1 — islanded black start. Baselines: 230 V, 50 Hz.

Metric	IAHO	VdP
Steady-state $V_{pcc,rms}$	229.98 V	229.96 V
Steady-state f_{osc}	50.0002 Hz	50.0000 Hz
V rise time (10–90%)	65 ms	123 ms
V_{rms} maximum	234.5 V	274.4 V
Voltage overshoot	+2.0%	+19.3%
V settling (±1%)	0.212 s	0.402 s
f_{osc} minimum	47.42 Hz	38.29 Hz
Peak |RoCoF| (100 ms)	33.7 Hz/s	117.1 Hz/s
f settling (±10 mHz)	0.546 s	0.245 s
$I_{L,RMS}$	7.2 A (0.16 pu)	7.2 A (0.16 pu)
Peak $\|i_L\|$ incl. ripple	16.1 A (0.26 pu)	16.5 A (0.27 pu)
Peak $\|v_{inv}\|$ command	330.6 V (1.02 pu)	387.9 V (1.19 pu)

Both reach the correct steady state, but not in the same manner. IAHO hits 90% voltage in 65 ms with 2.0% overshoot, against 123 ms and 19.3% for VdP. VdP frequency dips much further, to 38.29 Hz against 47.42 Hz, yet settles sooner (0.245 versus 0.546 s). Peak no-load currents are almost identical.

4.5 Islanded load step

A 0.5→1.0 pu resistive load step is applied at t = 2.000 s (Figure 8).

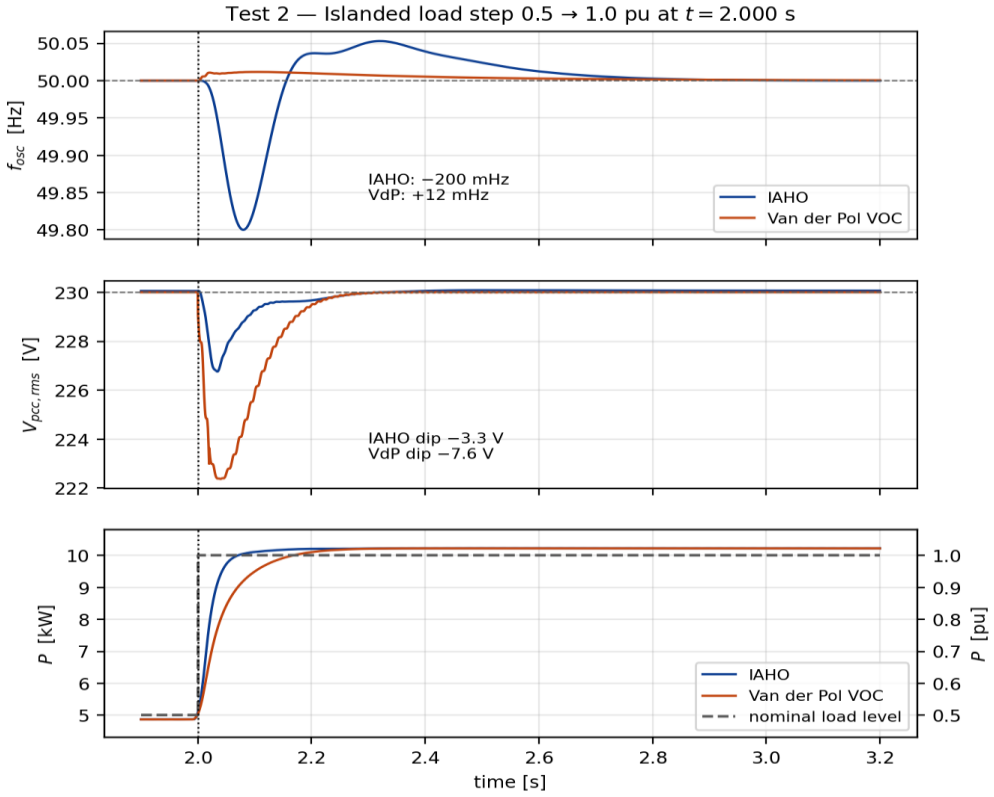


Figure 8 Frequency, PCC voltage and active power following the 0.5–1.0 pu islanded resistive load step at t = 2.000 s, IAHO against Van der Pol VOC.

Table 9 Test 2 — islanded load step, 0.5 to 1.0 pu. Baselines: 230 V, 50 Hz, 10 kW.

Metric	IAHO	VdP
P before → after	4.87 → 10.23 kW	4.87 → 10.22 kW
P rise time (10–90%)	44.8 ms	111.2 ms
P settling (±0.107 kW)	0.107 s	0.205 s
P overshoot	0.06%	0.01%
f_{osc} excursion	-200 mHz	+11.7 mHz
f settling (±10 mHz)	0.631 s	0.185 s
Peak |RoCoF| (20 ms)	4.66 Hz/s	0.56 Hz/s
Peak |RoCoF| (100 ms)	2.73 Hz/s	0.15 Hz/s
$V_{pcc,rms}$ minimum	226.8 V (-3.3 V)	222.4 V (-7.6 V)
V settling (±1.15 V)	0.085 s	0.168 s
Q transient peak	0.517 kvar	0.030 kvar
Peak |i_g| delivered	63.8 A (1.04 pu)	64.4 A (1.05 pu)
$I_{L,RMS}$ inverter loading	44.3 A (1.02 pu)	44.2 A (1.02 pu)
Peak |i_L| incl. ripple	74.5 A (1.21 pu)	78.4 A (1.27 pu)

Final power is the same in both cases; IAHO reaches the final value faster (44.8 ms rise, 0.107 s settling, against 111.2 ms and 0.205 s). The more important difference is the channel in which the disturbance appears. IAHO takes a 200 mHz frequency dip and a 3.3 V voltage dip, while VdP moves only 11.7 mHz in frequency but drops 7.6 V. Reactive cross-coupling is 0.517 kvar against 0.030 kvar, and delivered current is almost the same either way.

4.6 Pre-synchronisation and STS closure

Because the STS criterion is common to both, pre-synchronisation speed can be compared directly (Figure 9).

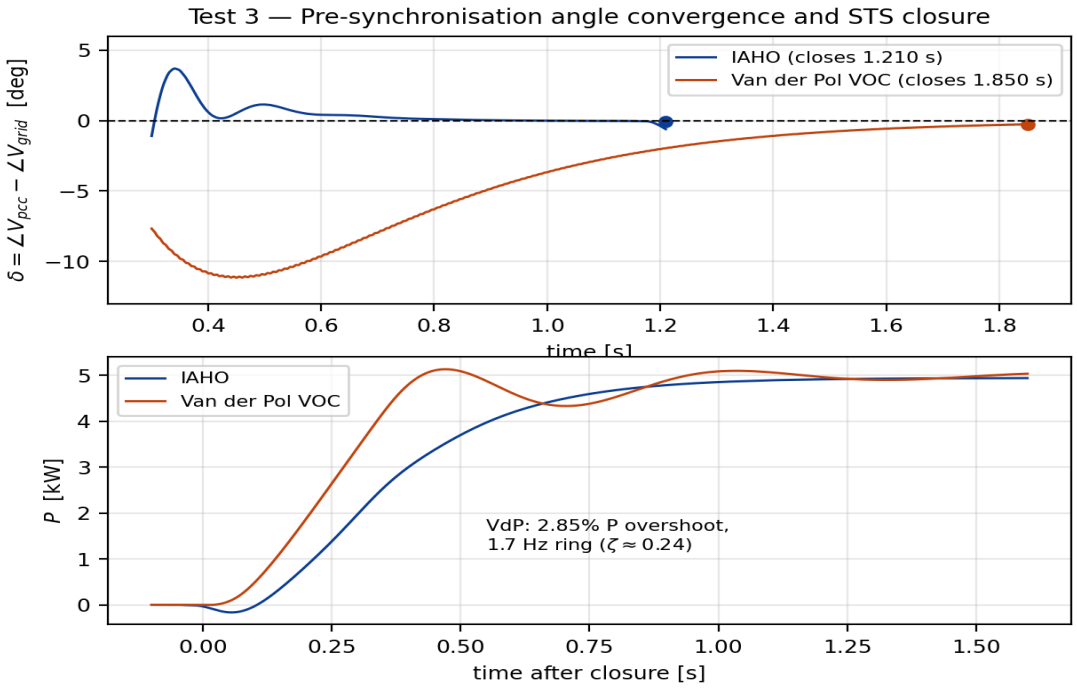


Figure 9 Pre-synchronisation and STS closure. Top: phase-angle error during pre-synchronisation, with closure marked (IAHO at t = 1.210 s, Van der Pol VOC at t = 1.850 s). Bottom: active power referred to the instant of closure.

Table 10 Test 3 — pre-synchronisation and STS closure. Latch thresholds identical: 2% voltage, 0.05 rad phase, 0.75 s hold.

Metric	IAHO	VdP
Time to STS closure	1.210 s	1.850 s
Angle error 30 ms pre-close	-0.065°	-0.295°
Frequency error pre-close	-0.93 mHz	+2.83 mHz
Voltage error pre-close	-0.023 V	+0.071 V
f deviation after closure	149.6 mHz	210.9 mHz
V deviation after closure	5.40 V	7.88 V
P overshoot	0.01%	2.85%
Q overshoot	0.01%	5.75%
Inrush peak $\lvert i_g \rvert$	34.2 A (0.56 pu)	38.1 A (0.62 pu)
$I_{L,RMS}$	25.1 A (0.58 pu)	27.7 A (0.64 pu)

Metric	IAHO	VdP
Inrush peak $\lvert i_L \rvert$	49.8 A (0.81 pu)	53.7 A (0.87 pu)
P settling	0.983 s	1.066 s
Post-closure V_{pcc}	235.0 V (+2.2%)	231.1 V (+0.5%)
Post-closure ringing	none detected	1.71 Hz, $\zeta \approx 0.24$

IAHO closes 0.64 s earlier (1.210 s against 1.850 s), with smaller pre-close errors and less inrush. VdP overshoots by 2.85% in P and 5.75% in Q and rings at 1.71 Hz after closure; nothing comparable is detectable for IAHO. In this heavily reactive case IAHO settles at 235.0 V, VdP at 231.1 V.

4.7 Grid-connected active-power step

The grid-connected reference is stepped 0.5→0.8 pu at 4.05 s and returned at 7.05 s (Figure 10).

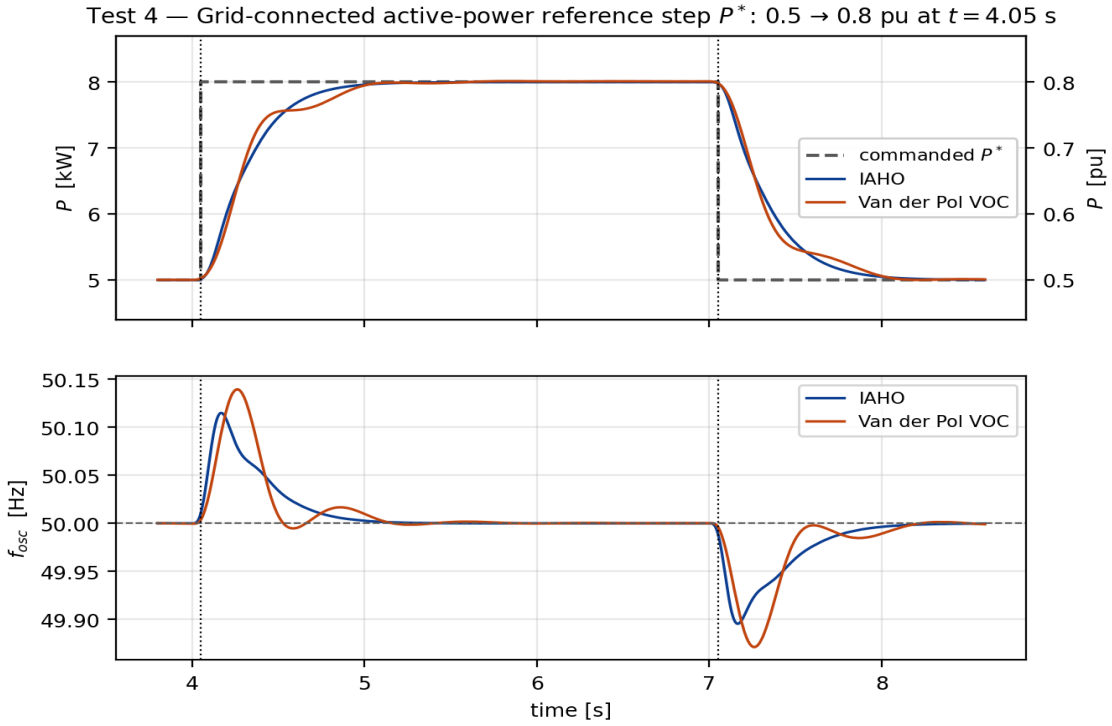


Figure 10 Grid-connected active-power reference step, P*: 0.5 -> 0.8 pu at t = 4.05 s and back at t = 7.05 s. Active power against the commanded reference, together with oscillator frequency, for IAHO and Van der Pol VOC.

Table 11 Test 4 — grid-connected active-power step. The commanded step is identical in both runs; the measured delivered step is 4% larger in the Van der Pol build, so power timings are compared as fractions of each measured step.

	Step up		Step down	
Metric	IAHO	VdP	IAHO	VdP
P step size	2.89 kW	3.01 kW	—	—
P rise (10–90%)	498 ms	652 ms	519 ms	627 ms
P overshoot	0.03%	0.14%	—	—
P settling	0.873 s	0.953 s	0.909 s	0.961 s

	Step up		Step down	
f max deviation	114.8 mHz	139.8 mHz	104.4 mHz	129.0 mHz
f settling	0.702 s	0.946 s	0.738 s	0.963 s
V max deviation	1.38 V	3.33 V	1.38 V	3.03 V
V settling	0.129 s	0.266 s	—	—
Peak |RoCoF| (100 ms)	1.12 Hz/s	0.91 Hz/s	—	—
Peak $\|i_g\|$ delivered	49.9 A	52.0 A	—	—
$I_{L,RMS}$	34.9 A	35.8 A	—	—
Ringing	none	1.48–1.67 Hz	none	1.36–1.66 Hz

IAHO tracks faster and produces smaller accompanying voltage and frequency deviations: 498 ms rise on the step up against 652 ms, 114.8 mHz frequency deviation against 139.8 mHz, and 1.38 V voltage deviation against 3.33 V. VdP rings at 1.4–1.7 Hz, while no such mode is detectable for IAHO.

4.8 Grid frequency disturbance

The grid frequency is stepped 50.0→49.5 Hz at 5.0 s and restored at 7.0 s (Figure 11); the applied source step itself has undefined RoCoF.

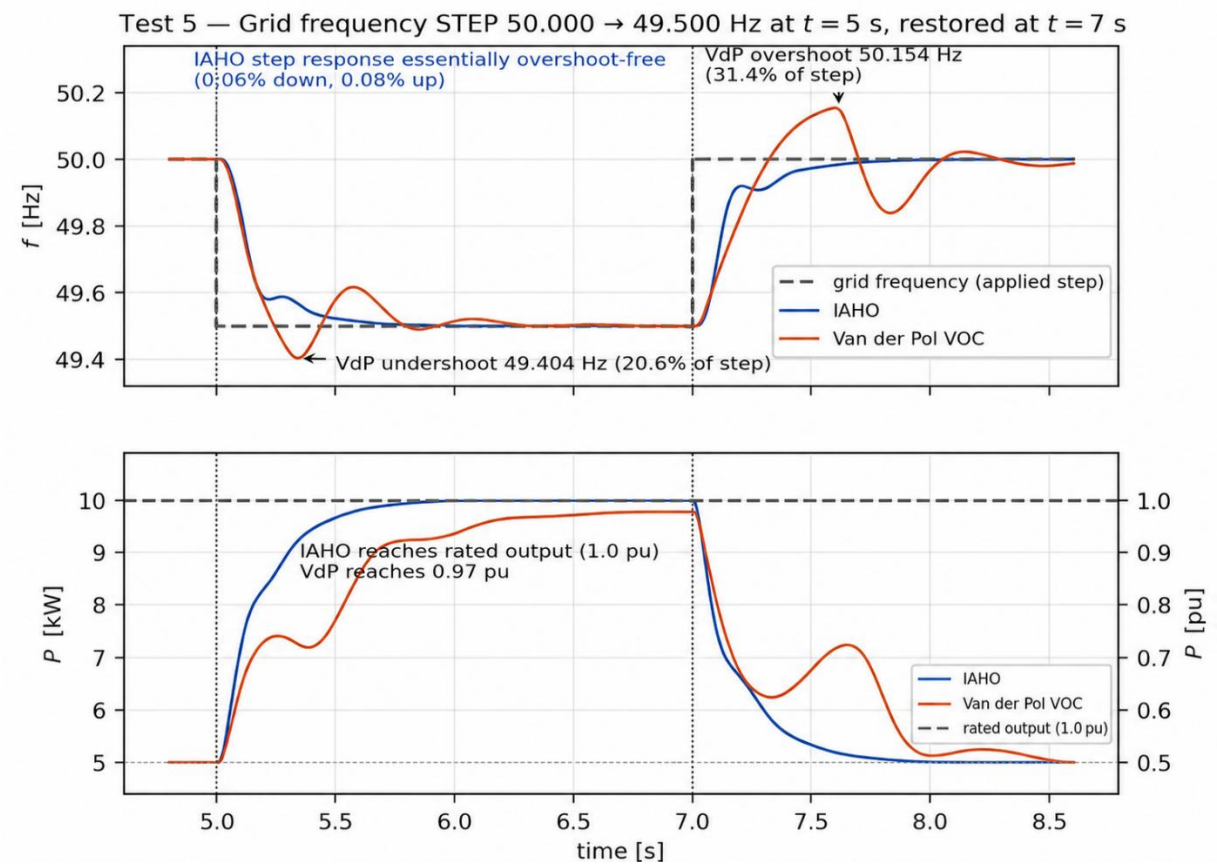


Figure 11 Response to a 50.000–49.500 Hz grid frequency step at t = 5.000 s, restored at t = 7.000 s. Oscillator frequency against the applied grid step, with delivered active power, for IAHO and Van der Pol VOC.

Table 12 Test 5 — grid frequency step, 50.000 to 49.500 Hz. Baseline: the commanded 49.500 Hz.

Metric	IAHO	VdP
Frequency drop		
f_{osc} minimum	49.5001 Hz	49.4040 Hz
Undershoot beyond target	0.06%	20.6%
f rise (10–90%)	312 ms	151 ms
f settling (±10 mHz)	0.640 s	1.162 s
Δ P delivered	+5.26 kW	+4.70 kW
P rise (10–90%)	379 ms	711 ms
P overshoot	0.07%	2.14%
V_{pcc} minimum	221.5 V	221.7 V
Peak |RoCoF| (100 ms)	3.45 Hz/s	3.18 Hz/s
$\left\lvert \int \Delta f \, dt \right\rvert$	0.9141 Hz·s	0.9192 Hz·s
Peak $\lvert i_g \rvert$ delivered	65.5 A (1.07 pu)	63.8 A (1.04 pu)
$I_{L,RMS}$ inverter loading	46.0 A (1.06 pu)	44.2 A (1.02 pu)
Peak $\lvert i_L \rvert$ incl. ripple	78.4 A (1.27 pu)	76.5 A (1.24 pu)
Frequency recovery		
f maximum	50.0002 Hz	50.1543 Hz
f overshoot	0.08%	31.4%
f settling	0.693 s	1.622 s
V_{pcc} maximum	235.3 V	243.7 V (+6.0%)
Q overshoot	0.00%	27.9%
Peak $\lvert v_{inv} \rvert$ command	1.040 pu	1.080 pu

IAHO is effectively overshoot-free, with 0.06% undershoot on the drop and 0.08% on recovery, where VdP swings to 49.404 Hz and 50.154 Hz. VdP moves faster at first and then takes longer to settle.

IAHO delivers +5.26 kW against +4.70 kW and builds that response in 379 ms rather than 711 ms, at 1.07 pu peak delivered current against 1.04 pu. The 5.4 mHz difference in final reported frequency is treated as measurement or readout bias, not as a real steady-state offset.

4.9 Grid voltage sag

The grid source is reduced to 0.70 pu for 3.00 s (Figure 12).

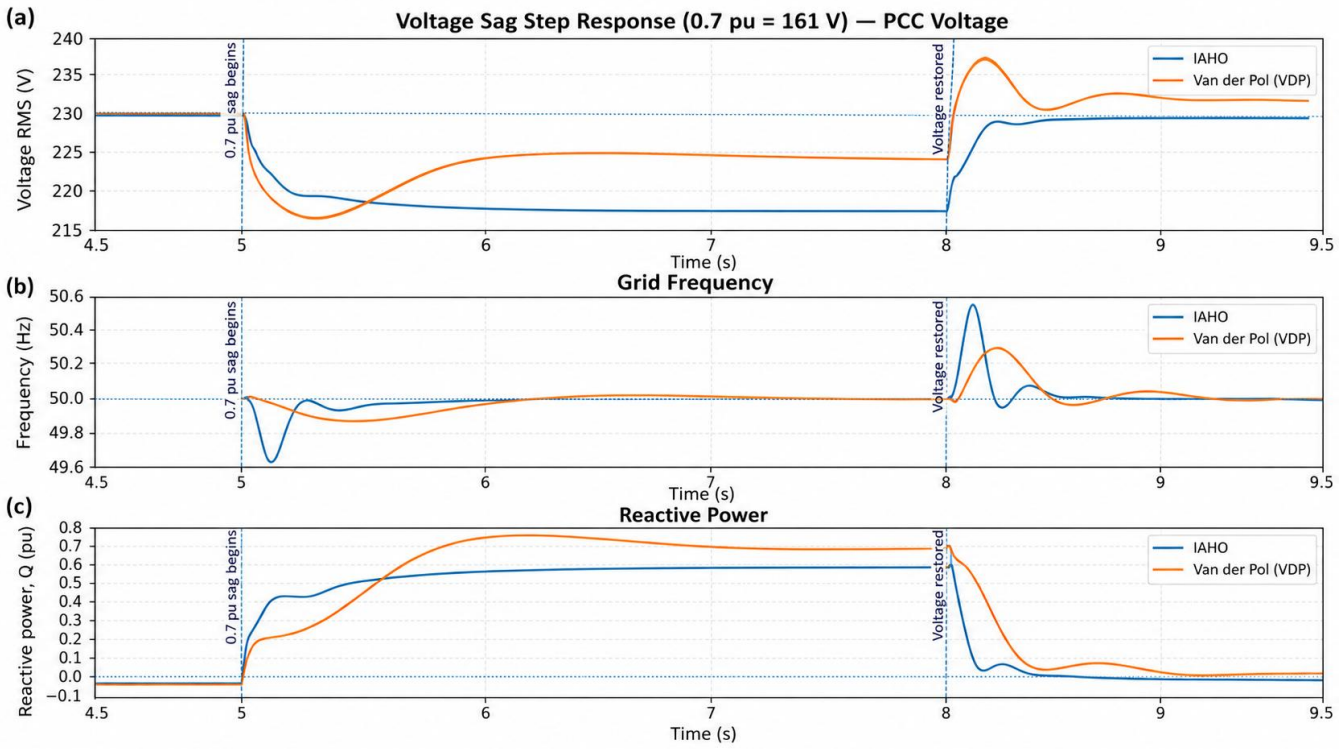


Figure 12 Response to a 0.70 pu grid voltage sag lasting 3.00 s: PCC voltage, reactive power and frequency, IAHO and Van der Pol VOC.

Table 13 Test 6 — grid voltage sag to 0.70 pu. Baselines: 230 V, 50 Hz, 5 kW pre-fault.

Metric	IAHO	VdP
During the sag		
V_{pcc} held	218.1 V (0.949 pu)	224.6 V (0.976 pu)
V_{pcc} minimum	218.1 V	217.1 V
Q injected (steady)	6.00 kvar	6.98 kvar
Q peak	6.10 kvar	7.52 kvar
P held	4.66 kW (-5.4%)	5.04 kW (+0.7%)
f_{osc} minimum	49.589 Hz (-411 mHz)	49.868 Hz (-132 mHz)
f settling	0.972 s	1.843 s
Peak |RoCoF| (100 ms)	5.04 Hz/s	0.51 Hz/s
Peak $\|i_g\|$ delivered	55.0 A (0.89 pu)	55.6 A (0.90 pu)
$I_{L,RMS}$	37.9 A (0.87 pu)	38.2 A (0.88 pu)
Power angle δ	-23.4°	-26.3°
After clearance		
V_{pcc} maximum	229.8 V	238.8 V (+3.8%)

Metric	IAHO	VdP
V settling	0.192 s	0.525 s
f_{osc} maximum	50.557 Hz (+557 mHz)	50.291 Hz (+290 mHz)
f settling	0.680 s	1.067 s
P minimum during recovery	1.18 kW	1.79 kW
Ringing	3.9–4.3 Hz, ζ = 0.22–0.31	1.6–3.1 Hz, ζ = 0.07–0.17

During the sag, VdP holds 224.6 V and injects 6.98 kvar, compared with 218.1 V and 6.00 kvar for IAHO, and it also exhibits the smaller frequency excursion. The VdP reactive-power injection reaches the 7 kvar volt–var limit; therefore, the sustained voltage-support advantage is attributed to the implemented controller configuration rather than to the Van der Pol oscillator alone. The IAHO 0.8→1.20 pu threshold sensitivity check again produced no noticeable waveform change.

After fault clearance, the relative performance changes. IAHO returns to 229.8 V with no overshoot and settles in 0.192 s, while VdP overshoots to 238.8 V and needs 0.525 s. The post-fault mode is also the better damped of the two for IAHO.

4.10 Low-order steady-state voltage harmonic content

The PCC-voltage spectrum is evaluated over a 50-cycle steady-state window before the dispatch step (Figure 13).

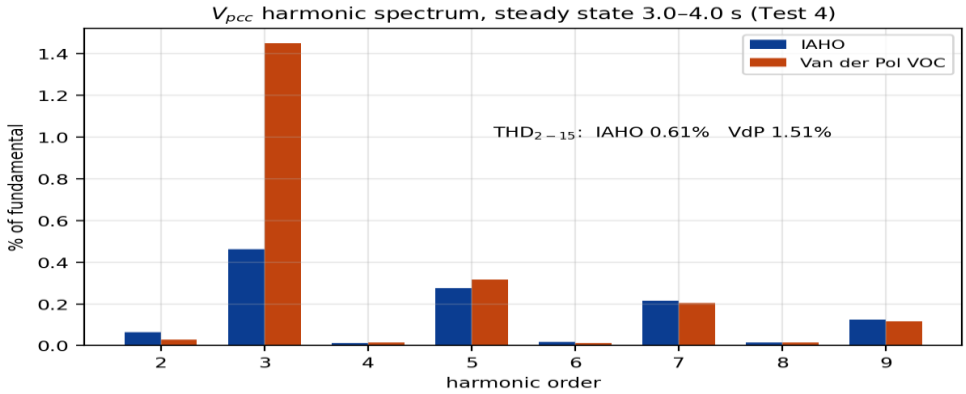


Figure 13 Steady-state PCC voltage harmonic spectrum, orders 2–9, as a percentage of the fundamental, for IAHO and Van der Pol VOC.

Table 14 Steady-state PCC voltage harmonics. The Van der Pol design target for the third harmonic was δ_{31} = 2%.

Harmonic	IAHO	VdP
3rd	0.464%	1.449%
5th	0.276%	0.317%
7th	0.216%	0.204%
Low-order voltage THD (harmonic orders 2–15)	0.610%	1.507%

VdP shows 1.449% third harmonic and 1.507% low-order voltage THD (harmonic orders 2–15), compared with 0.464% and 0.610% for IAHO. The VdP result remains below its 2% design

target, while the lower IAHO value is consistent with the absence of the Van der Pol cubic third-harmonic mechanism; it does not imply that the implemented inverter is harmonic-free.

4.11 Current stress and modulation utilisation

Table 15 separates delivered grid-side peak current from inverter-side RMS loading and from switching-ripple peaks.

Table 15 Current metrics across the six tests. Peak |ig| is the delivered current after the LCL filter; IL,RMS is inverter loading; peak |iL| includes switching ripple. Peak values in per unit of the 61.49 A peak base, RMS values of the 43.48 A RMS base.

Test	Peak $\lvert i_g \rvert$		$I_{L,RMS}$		Peak $\lvert i_L \rvert$	
	IAHO	VdP	IAHO	VdP	IAHO	VdP
1 — black start	—	—	0.16 pu	0.16 pu	0.26 pu	0.27 pu
2 — load step	1.04 pu	1.05 pu	1.02 pu	1.02 pu	1.21 pu	1.27 pu
3 — STS closure	0.56 pu	0.62 pu	0.58 pu	0.64 pu	0.81 pu	0.87 pu
4 — P^* step	0.81 pu	0.85 pu	0.80 pu	0.82 pu	1.02 pu	1.05 pu
5 — frequency step	1.07 pu	1.04 pu	1.06 pu	1.02 pu	1.27 pu	1.24 pu
6 — voltage sag	0.89 pu	0.90 pu	0.87 pu	0.88 pu	1.09 pu	1.11 pu

Differences in delivered current are small. The highest $I_{L,RMS}$ values recorded are 1.06 pu for IAHO and 1.02 pu for VdP. Raw i_L peaks run higher because of switching ripple, so they are not used to infer whether protection acted. On the evidence of the threshold sensitivity check, current limiting did not materially shape the reported responses.

VdP also requires greater voltage-command headroom, peaking at 1.19 pu of nominal AC peak against 1.04 pu for IAHO. Referred to the 500 V DC link, both stay under the common modulation clamp.

4.12 Overall performance summary

Table 16 collects the headline results across all six tests.

Table 16 Headline measured results across all tests.

Test	Quantity	IAHO	VdP
Black start	Voltage overshoot	+2.0%	+19.3%
Black start	Frequency excursion	-2.58 Hz	-11.71 Hz
Load step	Voltage dip	-3.3 V	-7.6 V
Load step	Frequency excursion	-200 mHz	+11.7 mHz
Load step	P rise time	44.8 ms	111.2 ms
Load step	Q cross-coupling	0.517 kvar	0.030 kvar
Sync	Time to closure	1.210 s	1.850 s
Sync	Inrush peak |iL|	0.81 pu	0.87 pu
P^* step	Rise time (up)	498 ms	652 ms

Test	Quantity	IAHO	VdP
P^* step	Voltage deviation	1.38 V	3.33 V
Freq. step	Undershoot beyond target	0.06%	20.6%
Freq. step	Δ P delivered	+5.26 kW	+4.70 kW
Freq. step	Frequency area	0.9141 Hz·s	0.9192 Hz·s
Voltage sag	PCC voltage held	218.1 V	224.6 V
Voltage sag	Reactive injected	6.00 kvar	6.98 kvar
Voltage sag	Post-fault V overshoot	0.0%	+3.8%
Harmonics	Low-order voltage THD (harmonic orders 2–15)	0.610%	1.507%
All tests	Peak inverter-voltage command	1.04 pu	1.19 pu
All tests	Peak delivered $\lvert i_g \rvert$	1.07 pu	1.05 pu
All tests	Peak $I_{L,RMS}$	1.06 pu	1.02 pu

5 Discussion

Section 4 reported what happened; this section explains why and separates differences arising from the oscillator structures from those arising from controller configuration.

Almost everything traces back to the power-channel pairing. Averaged, the VdP implementation routes P→V and Q→ω while IAHO routes P→ω and Q→V, which is why one disturbance lands in voltage for one controller and in frequency for the other.

$$P_\varphi = P\cos\varphi + Q\sin\varphi \quad (\text{drives amplitude}), \qquad Q_\varphi = Q\cos\varphi - P\sin\varphi \quad (\text{drives frequency}), \qquad (45)$$

5.1 Island-mode interpretation

The islanded load step makes this visible. VdP maintains tighter frequency regulation but experiences the larger voltage dip; IAHO accepts a controlled frequency transient and keeps voltage nearer nominal. The low VdP RoCoF is therefore not evidence of virtual inertia; active power is simply not routed to its primary frequency channel.

IAHO RoCoF, by contrast, is set by the chosen T_f and the droop design. Its 0.517 kvar of reactive cross-coupling says as much about the network as about the controller: at $R_T/X_T \approx 1$ the active and reactive channels are strongly coupled.

Black start highlights the effect of the nonlinear oscillator structures. Far from the limit cycle the VdP cubic keeps amplitude and phase coupled, while the AHO norm-based restoring term holds them apart. Part of the measured gap is still configuration: IAHO also runs a 50 ms soft-start ramp.

5.2 Grid-connected active-power interpretation

In grid-connected dispatch IAHO is faster, disturbs voltage less and shows no detectable lightly damped mode. That is what one would expect from synthesising $G_p(s)$ against a second-order damping target. The VdP outer PI keeps its 1.4–1.7 Hz mode.

5.3 Frequency-support interpretation

For the grid-frequency step, $G_\omega(s)$ together with the SOGI-FLL leaves IAHO essentially overshoot-free and quicker to settle. It also supplies 5.26 kW against 4.70 kW, though part of that gap is the 0.02 Hz VdP deadband rather than controller capability, and the extra support costs slightly more current.

5.4 Voltage-sag interpretation

The voltage-sag result cannot be read without the unmatched reactive-support configuration in mind.

VdP does sustain the higher PCC voltage during the sag, but its volt-var PI is saturated near 7 kVAr while IAHO relies only on its intrinsic Q–V droop. What the sustained sag compares, then, is two implemented configurations, not two oscillator cores.

The larger IAHO frequency excursion is structural. With P→ω pairing, a temporary frequency difference is the only way to move power angle during the sag.

$$\Delta\delta = 2\pi\int \left(f_{osc} - f_g\right)\mathrm{d}t. \qquad (46)$$

Once the fault clears the ordering reverses: IAHO shows no voltage overshoot, settles far faster and carries the more strongly damped post-fault mode.

5.5 Unexpected findings

Three results were not obvious beforehand. First, VdP can show the lower RoCoF while having no virtual inertia at all, because its active-power disturbance goes mainly to voltage. Second, changing T_f barely moves the IAHO dispatch rise time, since $G_p(s)$ is what sets that closed-loop bandwidth. Third, the final VdP frequency readout carries a small bias of ≈5.4 mHz in the frequency-step record, so millihertz-level settling comparisons deserve caution.

5.6 Influence of SOGI dynamics and frequency estimation

The SOGI matters dynamically in the IAHO because T_{so} = 9.0 ms is roughly a third of T_f. Its lag belongs inside the inertia and damping model, not outside it as an ideal measurement. The VdP outer frequency-support loop uses filtered PLL frequency instead.

5.7 Role of current protection

Protection is not implemented identically: IAHO uses a 1.20 pu virtual-impedance threshold on the fundamental current-vector magnitude (rated peak basis), whereas VdP retains its native 1.50 pu path. Raising the IAHO threshold from 0.8 to 1.20 pu produced no noticeable waveform change. Because limiter status was not exported, the instantaneous contribution of

the limiter cannot be isolated; protection is therefore not treated as a dominant source of the measured differences.

5.8 Grid-strength dependence and controller complexity

Only one weak, resistive tie was tested, so none of the coupling results should be carried over to stiffer or more inductive networks without checking. IAHO also has greater implementation complexity, adding a dedicated SOGI-QSG and FLL, resonant inertia and two network-dependent damping filters.

5.9 Controller selection and application suitability

Table 17 draws the main structural and implementation differences together.

Table 17 Structural and implementation comparison of the two controllers.

Feature	Van der Pol VOC	IAHO
Oscillator core	Van der Pol (cubic)	Andronov–Hopf (norm-based)
Grid-forming voltage	Yes	Yes
Intrinsic synchronisation after connection	Yes; explicit pre-STS phase loop	Yes; explicit pre-STS phase loop
Power-to-channel pairing	P→V, Q→ω	P→ω, Q→V
Explicit virtual inertia	None	Yes, T_f = 27.8 ms, H_{eq} = 0.69 s
Tunable feedforward damping	None	Yes, $G_p(s)$ and $G_\omega(s)$
Quadrature generation	Auxiliary SOGI-based measurement/synchronisation	Dedicated SOGI-QSG in primary αβ current path
Grid-frequency estimator	Grid PLL for pre-sync/readout and outer P–f support	SOGI-FLL for Gω(s); PLL for pre-sync/readout
Active-power droop	Outer P–f support, 2%, 0.02 Hz deadband	Intrinsic P–f droop, 2%, voltage-independent
Reactive/voltage control	Volt-var PI, 7 kVAr cap	Intrinsic Q–V droop only
Current limiting	Native current-protection path, 1.50 pu	Virtual-impedance limiter, 1.20 pu
Third-harmonic content	1.449% measured (cubic mechanism; no notch)	0.464% measured (no VdP cubic mechanism)
Implementation burden	Lower: simple primary oscillator + outer loops	Higher: SOGI-QSG/FLL, inertia and damping filters

Which controller to choose depends on the service required; Table 18 collects the measured trade-offs.

VdP suits simpler stand-alone duty, where islanded frequency must stay very tight and reactive cross-coupling low. IAHO is the better choice where synchronisation, grid-frequency support, damping, dispatch response and clean recovery after a disturbance are what matter.

Table 18 Controller suitability by application priority, taken from the measured results.

Application priority	Preferred	Basis
Tight islanded frequency regulation	VdP	11.7 mHz vs 200 mHz (pairing)
Small islanded voltage dip	IAHO	3.3 V vs 7.6 V dip
Fast islanded power delivery	IAHO	44.8 ms vs 111.2 ms rise
Low reactive cross-coupling	VdP	0.030 vs 0.517 kvar
Clean black start	IAHO	+2.0% vs +19.3% overshoot
Fast, accurate synchronisation	IAHO	1.21 s vs 1.85 s; 0.065° vs 0.295°
Grid dispatch tracking	IAHO	498 ms vs 652 ms; no ringing
Grid frequency support	IAHO	+5.26 vs +4.70 kW; 0.06% vs 20.6%
Damping of grid disturbances	IAHO	No detectable IAHO mode vs lightly damped VdP ringing
Sustained voltage support in a sag	VdP	224.6 V vs 218.1 V (configuration)
Clean post-fault recovery	IAHO	no overshoot vs +3.8%
Low voltage distortion	IAHO	0.61% vs 1.51% low-order THD (harmonic orders 2–15)
Low DC-link headroom	IAHO	1.04 pu vs 1.19 pu peak voltage command
Implementation simplicity	VdP	no FLL, damping synthesis or inertia tuning

Read these metrics with the underlying channel in mind. A small frequency deviation need not mean high inertia, and stronger grid support generally requires higher current.

6 Limitations and Future Work

The clearest limitation is that the grid-tied reactive-support structures and the VdP deadband were never matched, and the IAHO soft-start also influences the black-start comparison. A future core-to-core benchmark should equalise all three.

Validation is simulation-only. Sensor noise, dead time, computational delay and non-ideal switching will only appear under hardware-in-the-loop or laboratory testing.

Only one weak grid ($R_T/X_T = 1.05$, SCR ≈ 1.4) was tested. The alternative tie branches are already in the model and would support an R/X and SCR sensitivity study directly.

Only one inverter was studied, so parallel operation, power sharing and multi-inverter stability all remain open.

The 500 V DC source is ideal, which removes battery and DC-link energy limits from the picture entirely. A finite source with a state-of-charge model would be needed before any frequency-support claim could be called realistic.

Parameter sensitivity was explored only narrowly. A systematic sweep of the main VdP and IAHO tuning parameters, with the internal protection and reference channels logged directly, is a logical next step.

7 Conclusion

Van der Pol VOC and IAHO control were implemented and compared on one 10 kVA single-phase weak-grid PLECS platform. Their main structural difference is the power-channel pairing: VdP sends active-power disturbances mainly into voltage amplitude, whereas IAHO sends them into phase and frequency and additionally incorporates virtual inertia, feedforward damping and voltage-independent droop. IAHO synchronised 0.64 s faster, tracked dispatch faster, produced better-damped grid-connected dynamics, delivered stronger frequency support and reached lower low-order voltage THD (harmonic orders 2–15). VdP held islanded frequency tighter and kept reactive cross-coupling lower, and its stronger sustained support during the voltage sag is strongly influenced by the enabled volt-var loop.

For the system tested, VdP fits simpler stand-alone duty, while IAHO is the stronger choice wherever repeated grid connection, ancillary frequency support and recovery from disturbances are required. These conclusions are specific to the simulation; matched reactive support, a range of grid strengths and hardware validation are the natural next tests.

References

[1] H. Rezazadeh, M. Monfared, M. Fazeli, and S. Golestan, "IAHO: Integrated Andronov–Hopf oscillator for providing ancillary services with single-phase grid-forming inverters," *Electric Power Systems Research*, vol. 254, p. 112625, 2026, doi: 10.1016/j.epsr.2025.112625.

[2] H. Rezazadeh, M. Monfared, M. Fazeli, and S. Golestan, "Single-phase grid-forming inverters: A review," in *2023 international conference on computing, electronics & communications engineering (iCCECE)*, IEEE, Aug. 2023, pp. 7–10. doi: 10.1109/iCCECE59400.2023.10238661.

[3] B. B. Johnson, S. V. Dhople, A. O. Hamadeh, and P. T. Krein, "Synchronization of parallel single-phase inverters with virtual oscillator control," *IEEE Transactions on Power Electronics*, vol. 29, no. 11, pp. 6124–6138, 2014, doi: 10.1109/TPEL.2013.2296292.

[4] M. A. Awal, H. Yu, H. Tu, S. M. Lukic, and I. Husain, "Hierarchical control for virtual oscillator based grid-connected and islanded microgrids," *IEEE Transactions on Power Electronics*, vol. 35, no. 1, pp. 988–1001, Jan. 2020, doi: 10.1109/TPEL.2019.2912152.

[5] M. Lu, "Virtual oscillator grid-forming inverters: State of the art, modeling, and stability," *IEEE Transactions on Power Electronics*, vol. 37, no. 10, pp. 11579–11591, Oct. 2022, doi: 10.1109/TPEL.2022.3163377.

[6] B. B. Johnson, M. Sinha, N. G. Ainsworth, F. Dörfler, and S. V. Dhople, "Synthesizing virtual oscillators to control islanded inverters," *IEEE Transactions on Power Electronics*, vol. 31, no. 8, pp. 6002–6015, Aug. 2016, doi: 10.1109/TPEL.2015.2497217.

[7] M. Lu, S. Dutta, V. Purba, S. Dhople, and B. Johnson, "A grid-compatible virtual oscillator controller: Analysis and design," in *2019 IEEE energy conversion congress and exposition (ECCE)*, IEEE, Sep. 2019, pp. 2643–2649. doi: 10.1109/ECCE.2019.8913128.

[8] D. Raisz, T. T. Thai, and A. Monti, "Power control of virtual oscillator controlled inverters in grid-connected mode," *IEEE Transactions on Power Electronics*, vol. 34, no. 6, pp. 5916–5926, 2019, doi: 10.1109/TPEL.2018.2868996.

[9] M. A. Awal and I. Husain, "Unified virtual oscillator control for grid-forming and grid-following converters," *IEEE Journal of Emerging and Selected Topics in Power Electronics*, vol. 9, no. 4, pp. 4573–4586, Aug. 2021, doi: 10.1109/JESTPE.2020.3025748.

[10] S. Luo, W. Chen, X. Li, and Z. Hao, "A new virtual inertial strategy for Andronov–Hopf oscillator based grid-forming inverters," *IEEE Journal of Emerging and Selected Topics in Power Electronics*, vol. 12, no. 2, pp. 1995–2005, Apr. 2024, doi: 10.1109/JESTPE.2024.3370171.

[11] H. Rezazadeh, M. Monfared, M. Fazeli, and S. Golestan, "Enhancing damping in single-phase grid-forming virtual oscillator control inverters: A feedforward strategy," *IEEE Open Journal of the Industrial Electronics Society*, vol. 6, pp. 1101–1115, Jul. 2025, doi: 10.1109/OJIES.2025.3588677.

[12] H. Rezazadeh, M. Monfared, M. Fazeli, and S. Golestan, "Voltage-independent active-power droop coefficient for enhanced Andronov–Hopf oscillator grid-forming inverters." Nov. 2025. doi: 10.48550/arXiv.2511.05252.

[13] H. Rezazadeh, M. Monfared, M. Fazeli, and S. Golestan, "Virtual oscillator control for grid-forming inverters: Recent advances, comparative evaluation, and small-signal analysis," *Energies*, vol. 18, no. 22, p. 5981, 2025, doi: 10.3390/en18225981.

[14] M. Ciobotaru, R. Teodorescu, and F. Blaabjerg, "A new single-phase PLL structure based on second order generalized integrator," in *2006 37th IEEE power electronics specialists conference*, IEEE, Jun. 2006, pp. 1–6. doi: 10.1109/pesc.2006.1711988.

[15] S. Golestan, J. M. Guerrero, J. C. Vasquez, A. M. Abusorrah, and Y. Al-Turki, "Standard SOGI-FLL and its close variants: Precise modeling in LTP framework and determining stability region/robustness metrics," *IEEE Transactions on Power Electronics*, vol. 36, no. 1, pp. 409–422, Jan. 2021, doi: 10.1109/TPEL.2020.2997603.